

**HAZARD CONSISTENT SEISMIC PERFORMANCE ASSESSMENT
OF ROCKFILL DAMS**

A Dissertation
Presented to
The Academic Faculty

by

Venkataraman Ramesh

In Partial Fulfillment
of the Requirements for the Degree
Master of Science in the
School of Civil and Environmental Engineering

Georgia Institute of Technology
May 2021

COPYRIGHT © 2021 BY VENKATARAMAN RAMESH

HAZARD CONSISTENT SEISMIC PERFORMANCE ASSESSMENT OF ROCKFILL DAMS

Approved by:

Dr. Jorge Macedo, Advisor
School of Civil and Environmental Engineering
Georgia Institute of Technology

Dr. J. David Frost
School of Civil and Environmental Engineering
Georgia Institute of Technology

Dr. Gabriel Candia
Facultad de Ingeniería Civil
Universidad del Desarrollo, Chile

Date Approved: Jan 23rd, 2021

ACKNOWLEDGEMENTS

I would like to express my sincere gratitude to my advisor, Professor Jorge Macedo for his mentorship and guidance throughout this course of work. I feel extremely lucky to have had the chance to work with him during my time at Georgia Tech. Dr. Macedo's passion for teaching and knack to explain concepts helped me to get a firm hold on to the fundamentals of earthquake geotechnical engineering. Dr. Macedo's guidance not only helped me become a better engineer but also a better person. I would also like to thank Dr. Gabriel Candia for facilitating information to implement the Probabilistic Seismic Displacement Analysis platform used in Chapter 4.

I am also grateful to Geosystems faculty member at Georgia Tech: Professors Paul Mayne, Chloe Arson, David Frost, Sheng Dai. They have provided a great foundation for my future endeavors. I would like to thank my fellow Geosystems students for providing a welcoming and supportive environment. Special thanks to Shaivan, Luis Vergaray, Cody Arnold, Mohammad Zaid and Chenying Liu.

I am extremely thankful to my parents and my brother, for supporting me and encouraging me throughout my life. Without them, I would not be where I am today.

Lastly, I would like to thank my friends Siddharth and Sreepraneeth for helping me keep my spirit up throughout my time at Georgia Tech.

TABLE OF CONTENTS

ACKNOWLEDGEMENTS	iii
LIST OF TABLES	v
LIST OF FIGURES	vi
SUMMARY	ix
CHAPTER 1. Introduction	1
CHAPTER 2. Literature Review	6
2.1 Seismic assessment of slope systems and dams	6
2.1.1 Key design issue	6
2.1.2 Analytical procedures	6
2.1.3 Probabilistic seismic displacement analysis using predictive models	10
2.1.4 Estimation of seismically-induced slope displacements using a stick-slip model (Rathje and Bray, 2000)	11
2.1.5 Transfer function model (Hale, 2019)	12
2.2 Dynamic Response of Rockfill Materials	14
CHAPTER 3. Selection Of Ground Motion Time Histories	20
3.1 Probabilistic Seismic Hazard Analysis	20
3.2 Ground-motion Database	24
3.3 Conditional Scenario Spectra	27
3.4 Selected Scenario Spectra	32
CHAPTER 4. Performance-Based Seismic Assessment Using Analytical Methods	36
4.1 Evaluation of Seismic Yield Coefficient	36
4.2 Probabilistic Seismic Displacement Analysis (PSDA)	39
4.3 Stick-slip Model	42
4.4 Transfer Function Model	44
4.5 Displacement Hazard Curves	47
CHAPTER 5. Dynamic Analysis	52
5.1 Dam geometry	52
5.2 Calibration of Constitutive Models	52
5.2.1 UBCHyst	54
5.2.2 PM4 Sand	56
5.2.3 Wang 2D model	58
5.3 Static Analysis	60
5.4 Dynamic Analysis	63
CHAPTER 6. Results From dynamic Analysis	64
6.1 Comparison of Constitutive Models	64
6.1.1 PGA vs Displacement	64
6.2 Displacement Hazard Curves	65
6.3 Comparison with analytical procedures	73
CHAPTER 7. Summary of findings and Conclusions	76
REFERENCES	80

LIST OF TABLES

Table 1	- Mean magnitude and distance contributing to all selected hazard levels for a period of 0.5 seconds obtained from hazard deaggregation	24
Table 2	- Material properties used for different layers for analysis in SLIDE	37
Table 3	Different layers based on confinement	53
Table 4	Comparison of displacements for a selected return period.	74

LIST OF FIGURES

Figure 1-1	Different approaches for the estimation of EDPs; where ϵ_{GM} is the number of standard deviation below and above the median IM , λ_{GM} is the mean annual rate of exceedance of the IM , ϵ_d is the number of standard deviation below and above the median displacement, λ_d is the mean annual rate of exceedance of displacement.	3
Figure 2-1	Calculation of seismically-induced displacements using Newmark-type procedure.	8
Figure 3-1	Four steps involved in a probabilistic seismic hazard analysis (Kramer, 1996)	21
Figure 3-2	Mean hazard curves obtained from PSHA	22
Figure 3-3	Uniform hazard spectrum obtained from PSHA	23
Figure 3-4	Deaggregation of the seismic hazard at the selected site for spectral period of 0.5 seconds for a return period of 100 years	23
Figure 3-5	Magnitude-distance distribution of the selected subset	25
Figure 3-6	Distribution of PGA in the selected subset	25
Figure 3-7	Distribution of Arias Intensity in the selected subset	26
Figure 3-8	Distribution of V_{S30} in the selected subset	26
Figure 3-9	Conditional mean spectra constructed for all selected hazard	28
Figure 3-10	Set of time histories selected and scaled based on CMS and its variability for a hazard level of 1.00E – 2	29
Figure 3-11	Flow chart illustrating the steps involves in CSS	31
Figure 3-12	Hazard curve recovered from CSS for a spectral period of 0.5 seconds	32
Figure 3-13	Magnitude-distance distribution for the selected ground motions	33
Figure 3-14	Distribution of PGA for the selected ground motions	34
Figure 3-15	All selected scenario spectra from CSS	34
Figure 3-16	Final rate of occurrence for each spectrum	35
Figure 3-17	Comparison of target uniform hazard spectrum from PSHA and uniform hazard spectrum recovered from CSS	35
Figure 4-1	Geometry of the dam and different layers	37
Figure 4-2	Slip Surfaces for yield coefficient value of 0.12	38
Figure 4-3	Slip Surfaces for yield coefficient value 0.15	38
Figure 4-4	Slip Surfaces for yield coefficient value 0.2	39

Figure 4-5	Snapshot from PSDA2 platform showing different branches and weights for a mean K_y value of 0.12	40
Figure 4-6	All fractiles of displacement hazard curves and weighted mean obtained from PSDA2 for a mean K_y value of 0.12.	41
Figure 4-7	All fractiles of displacement hazard curves and weighted mean obtained from PSDA2 for a mean value K_y of 0.15.	41
Figure 4-8	All fractiles of displacement hazard curves and weighted mean obtained from PSDA2 for a mean value K_y of 0.2.	42
Figure 4-9	(a) Input PGA and displacements, (b) Arias Intensity and displacements obtained from stick-slip model for different K_y values.	43
Figure 4-10	(a) Input PGA and displacements, (b) Arias Intensity and displacements obtained from Transfer function model for different K_y values.	45
Figure 4-11	Comparison of displacements obtained from transfer function model and stick-slip model for a K_y value of 0.15.	46
Figure 4-12	Comparison of (a) displacement hazard curves (b) histograms of displacements (c) summed rate occurrences for displacement bins obtained from analytical procedures for a K_y value of 0.12.	49
Figure 4-13	Comparison of (a) displacement hazard curves (b) histograms of displacements (c) summed rate of occurrences for displacement bins obtained from analytical procedures for a K_y value of 0.15.	50
Figure 4-14	Comparison of (a) displacement hazard curves (b) histograms of displacements (c) summed rate of occurrences for displacement bins obtained from analytical procedures for a K_y value of 0.2.	51
Figure 5-1	Numerical Mesh and the dam model.	52
Figure 5-2	UBCHYST model key variables (Byrne and Naesgaard, 2015).	54
Figure 5-3	Calibrated modulus reduction and damping curves for UBCHyst model.	56
Figure 5-4	Schematic of yield, critical, dilatancy and bonding lines in q-p space. (from Boulanger and Ziotopolou, 2017).	57
Figure 5-5	Calibrated modulus reduction and damping curves for PM4Sand model.	58

Figure 5-6	Calibrated modulus reduction and damping curves for Wang2D model.	60
Figure 5-7	Initial static vertical stress contours.	61
Figure 5-8	Initial static horizontal stress contours.	62
Figure 5-9	Initial static pore pressure contours.	62
Figure 6-1	Horizontal displacement at a point in the downstream slope and input PGA.	64
Figure 6-2	Vertical displacement in the crest area and input PGA.	65
Figure 6-3	Horizontal displacement hazard curves at a point in the downstream slope from dynamic analysis.	66
Figure 6-4	Vertical displacement hazard curves in the crest area from dynamic analysis.	67
Figure 6-5	Median and maximum total displacement hazard curves for all three constitutive models.	68
Figure 6-6	Modulus reduction and damping curves for Layer 3.	70
Figure 6-7	Modulus reduction and damping curves for Layer 5.	71
Figure 6-8	Results from cyclic direct simple shear test for Layer 3.	71
Figure 6-9	Results from cyclic direct simple shear test for Layer 5.	72
Figure 6-10	Modulus reduction and damping curves for a confinement of 10 kPa.	72
Figure 6-11	Results from cyclic direct simple shear test for a confinement of 10 kPa.	73
Figure 6-12	Comparison of displacement hazard curves from analytical methods and nonlinear dynamic analyses.	75

SUMMARY

Slope systems such as earth/rockfill dams, waste storage landfill, or natural slopes can undergo significant damage during a seismic event. In the seismic design of slope systems, engineers often consider the amount of seismically-induced displacements as the key engineering demand parameter. The current state of practice procedures to estimate seismically-induced slope displacements are dominated by deterministic or pseudo-probabilistic approaches that do not directly quantify the hazard associated with the estimated displacements. Instead, these approaches assume that the hazard of the ground motion intensity measure of interest (e.g., peak ground acceleration) also represents the hazard of the estimated displacements. In contrast, performance-based approaches, which are the focus of this study, can provide hazard curves for the engineering demand parameter of interest (i.e., the amount of seismically-induced displacements in the context of this study), from which the estimated displacements can be directly related to the hazard design level.

In this study, we propose to combine the conditional scenario spectra approach with advanced numerical modeling as a benchmark to evaluate performance-based approaches that rely on simplified and analytical procedures for the estimation of seismically-induced displacements in rockfill dams. The evaluations show that the displacement hazard curves obtained through computationally intensive numerical analyses (performed with three different constitutive models) are more conservative than the hazard curves from simplified or analytical methods. Insights from the comparisons are shared, and potential explanations for the differences are provided. Finally, there are also differences in the displacement

hazard curves estimated through numerical analyses, which depend on the trade-off of volumetric/deviatoric mechanisms and damping in each constitutive model.

CHAPTER 1. INTRODUCTION

Dams are one of the most significant components in modern infrastructure as they maximize the usefulness of water resources, prevent potential flood-induced damages, and manage drought effects. Dams are also used in the mining industry to retain waste materials such as mine tailings. Though dams are essential, they also present a potential hazard; indeed, several case histories have shown the devastating effects that a dam failure could cause. Moreover, even in cases without a catastrophic failure, significant damage of a dam can still have severe economic consequences. For example, in 1971, the failure of San Fernando dam forced 80,000 people to vacate their residences (Seed et al., 1973).

In terms of seismic design, to keep the functionality of a dam system, the integrity of their slopes (and other components, such as the filters and drains) needs to be preserved during a seismic event. In particular, the potential damage to the crest and upstream/downstream slopes are of concern. In general, earthquake-induced damage to slope systems (e.g., natural slopes, dams, landfills, etc.) have caused severe disruptions in infrastructure systems during previous earthquakes. For example, during the 1964 Alaska earthquake, more than half of the total cost of damage was caused by earthquake-induced slope displacements, such as landslides (Youd, 1978; Wilson and Keefer, 1985). Hence, the adequate design of a dam slope is key in dam engineering.

In the current state of practice, the seismic design of earth and rockfill dams relies on the estimation of intensity measure parameters (*IMs*), which serve as proxies for the amplitude,

frequency content, and duration of a ground motion. For example, the most commonly used *IM* to represent the amplitude of a ground motion is the peak ground acceleration (*PGA*), which is simply the absolute largest acceleration of the ground-motion acceleration time history. There are also other *IMs* such as cumulative absolute velocity (*CAV*), Arias Intensity (I_a) that represents all three characteristics (amplitude, frequency content, duration) of an acceleration time history and have proven to be beneficial in the design of earth structures and geotechnical systems (Bray and Macedo, 2017; Macedo et al., 2020; Macedo, Abrahamson, Liu, 2020).

To quantitatively assess the possible damage an earthquake might cause to a certain structure, several analytical models have been developed to provide estimates of engineering demand parameters (*EDPs*), which can be used to assess the seismic performance of an engineering system. For dam structures, the *EDP* of interest to assess the seismic performance is often the amount of seismically induced slope displacement, which will be evaluated in this study through various procedures, considering different analytical models and advanced numerical modeling.

As illustrated in Figure 1-1, the current state of practice considers three different frameworks for the estimation of engineering demand parameters (*EDPs*), which in the context of this study corresponds to the amount of seismically-induced slope displacement. These frameworks are, 1) Deterministic, 2) Pseudo-probabilistic, 3) Performance-based probabilistic approach. These frameworks are usually used in combination with robust probabilistic models that estimate seismically induced slope displacements (discussed in the next chapter).

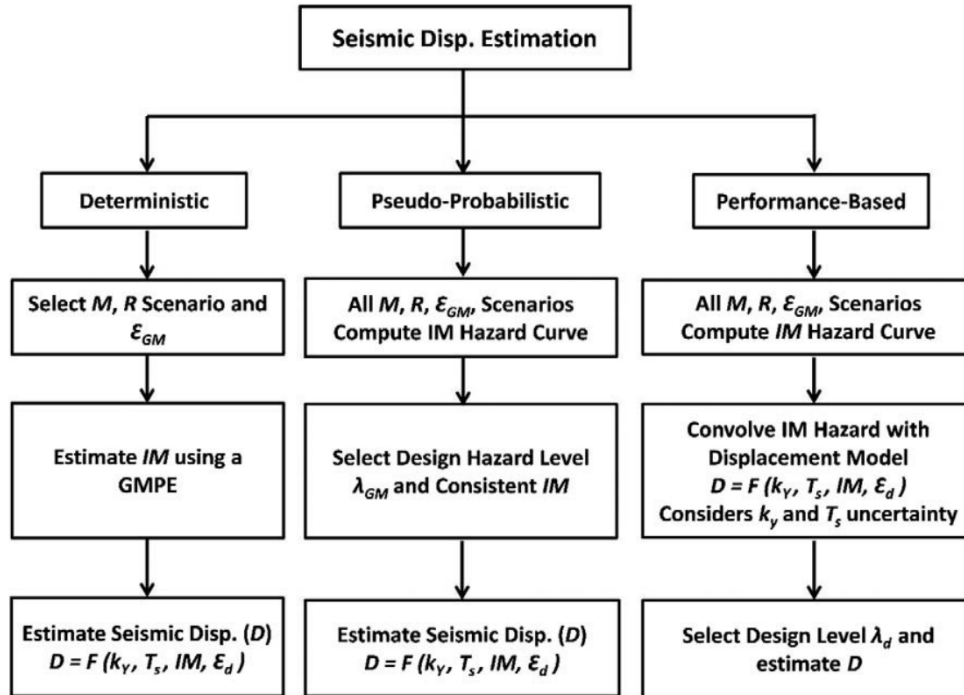


Figure 1-1 Different approaches for the estimation of EDPs; where ϵ_{GM} is the number of standard deviation below and above the median IM , λ_{GM} is the mean annual rate of exceedance of the IM , ϵ_d is the number of standard deviation below and above the median displacement, λ_d is the mean annual rate of exceedance of displacement.

In a deterministic approach, a design earthquake scenario, defined by magnitude (M) and distance (R) is selected. The IM is estimated using the ground motion prediction equation ($GMPE$). Then the seismic displacement can be calculated using an analytical model. In this approach, both the variability in the estimation of IM and system properties (the yield coefficient, K_y or the fundamental period, T_s) are not considered.

In a pseudo-probabilistic approach, the ground motion IM is estimated probabilistically through probabilistic seismic hazard analysis ($PSHA$) from which an IM hazard curve is constructed. The design IM value is selected from the hazard curves based on a design hazard level. This IM value is then used to estimate the amount of seismically-induced displacements. Here, only the IM is calculated probabilistically, and displacement is not.

The *EDP* hazard is estimated with the underlying assumption that the hazard level for displacement is consistent with that of *IM*.

In a performance-based model, the variability in both ground motion *IM* and seismically-induced displacement are considered. Several fractiles of *IM* hazard curves can be considered, which are convolved with a seismic displacement model and the variability of the system properties used in the model. Different displacement models can be used to account for epistemic uncertainties associated with the estimation of seismically-induced slope displacements. The result is an *EDP* hazard curve, which provides the mean rate of exceedance for different *EDP* levels. This curve can be used to estimate the expected level of displacement for the desired hazard level and is well suited to make engineering decisions. Moreover, the assumption that the *IM* hazard is consistent with the hazard associated with seismically-induced displacement is not needed anymore, which is more consistent with performance-based earthquake engineering concepts.

In this study, we extend the performance-based framework by integrating advanced numerical modeling, considering a large set of ground-motion time histories that are selected to be consistent with prescribed hazard design levels, obtained from probabilistic seismic hazard analyses (*PSHA*). The proposed procedure in this study also produces a hazard curve for the *EDP* of interest (i.e., the amount of seismically-induced slope displacements, in the context of this study). However, this study has the advantage of estimating these curves directly from advanced numerical modeling; hence, incorporating the physics associated to the generation of seismically-induced slope displacements more completely.

The content of this thesis is described as follows:

Chapter 1 presents an introduction to the study and highlights the overall objective of this study.

Chapter 2 presents a literature review on the assessment of the seismic performance of rockfill dams.

Chapter 3 presents the selection of ground motions using the conditional scenario approach, which will be used later in dynamic analyses.

Chapter 4 presents the results obtained using analytical models for the estimation of seismically-induced slope displacements for an existing rockfill dam.

Chapter 5 presents the constitutive models used in this study and the details of the numerical dynamic analyses performed on the same dam evaluated in chapter 4.

Chapter 6 presents the results from the dynamic analysis, including the generation of displacement hazard curves and the comparison of results with analytical models used in the current state of practice

Chapter 7 presents the main findings and conclusions from this study.

CHAPTER 2. LITERATURE REVIEW

2.1 Seismic assessment of slope systems and dams

In the current state of practice, the seismic evaluation of slope systems ranges from using relatively simple pseudo-static procedures (e.g., Macedo and Candia, 2020; Macedo and Candia, 2019a, 2019b) to advanced nonlinear finite element or finite difference methods (Macedo and Aguilar, 2011, 2012; Macedo et al., 2010, 2015).

2.1.1 *Key design issue*

It is important to address a key design criterion that should be considered before evaluating the seismic performance of an earth structure. We should first assess if there are materials in the structure or foundation that can lose significant strength as a result of cyclic loading (e.g., soil liquefaction). If that is the case, this should be the primary focus of the evaluation because it may lead to large displacement flow slides. There are various methods to estimate liquefaction-induced displacements (e.g., Macedo, 2017; Bray and Macedo, 2017a, 2017b; Macedo and Bray, 2018a, 2018b; Bray and Macedo, 2018a, 2018b, 2018c; Bray et al., 2017) which are not the focus of this study. If the materials within or below the earth structure will not lose significant strength as a result of seismic loading and if the structure will undergo significant deformation that may lead to potential damage, the estimation of seismically induced displacement helps in addressing this issue, which is the main focus of this study.

2.1.2 *Analytical procedures*

The seismic stability of earth and waste storage structures are commonly evaluated through the Newmark-type sliding block analyses that provide an estimate of the expected amount of seismically-induced slope displacements. Newmark (1965) proposed a procedure that models the sliding mass as a rigid block to calculate seismically induced displacement based on two parameters: yield acceleration (K_y) and input acceleration time-history. Sliding begins when the yield acceleration is exceeded and continues until the sliding block and foundation velocity coincides. The displacement is obtained by integrating the relative velocity between the rigid block and its foundation. This procedure illustrated in Figure 2-1: a) shows the acceleration time history with the threshold K_y , displacement occurs when acceleration amplitude crosses this threshold; b) shows the velocity-time history obtained by integrating the acceleration that causes displacement; c) shows the displacement time history obtained by integrating the calculated velocity time history. In addition to the shear-induced displacement, the top of a slope can displace downward due to deviatoric deformation or volumetric compression of the materials. This ground movement resulting from volumetric compression is not explicitly captured by Newmark-type models. As discussed in Stewart et al. (2001), although in some cases Newmark-type models appear to capture the overall amount of seismically-induced slope displacement in cases where the displacement is dominated by volumetric compression, that is because the seismic forces that cause high volumetric compression also result in large shear-induced deformations, in other words, it is just circumstantial. When analytical procedures are employed, deviatoric induced deformations and volumetric-induced deformations should be analyzed separately by using appropriate procedures. Tokimatsu and Seed (1987) could be used to estimate volumetric-induced deformation.

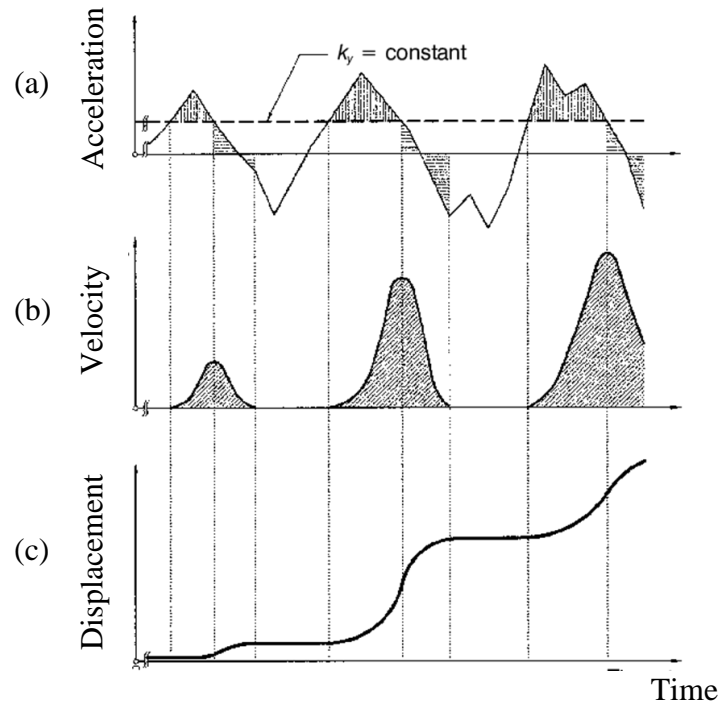


Figure 2-1 Calculation of seismically-induced displacements using Newmark-type procedure.

The Newmark (1965) procedure was later modified by Makdisi and Seed (1978) to take into account the deformable response of the structure. In their proposed method, dynamic analyses were performed, and the seismic coefficient-time history calculated from each analysis is later used to calculate the sliding response. This is called decoupled analysis. The procedure is based on a very limited number of dynamic analyses. But as they recommend, their results should be updated as the profession advances.

Bray and Travasarou (2007) proposed a predictive relationship for estimating earthquake-induced permanent shear displacements. It is based on a fully coupled, nonlinear, deformable stick-slip model to capture the dynamic performance of the earth system. The ground motion database used for this study to generate seismic displacements included 688 shallow crustal earthquake records with eight sliding block systems with a fundamental period varying from 0 – 2.0 s and yield coefficient ranging from 0.02 – 0.4. Seismically-

induced displacements are estimated from the initial fundamental period (T_s), the spectral acceleration of the ground motion at a degraded period of 1.5 times the fundamental period ($S_{a1.5T_s}$), the magnitude of the earthquake (M_w), and the yield coefficient (K_y).

Rathje et al. (2014) used the models of Saygili and Rathje (2008) as well as Rathje and Saygili (2009) and studied the probabilistic assessment of seismic slope displacement using both scalar hazard (i.e., using one ground motion parameter, PGA) and vector hazard (using two ground motion parameters, PGA and peak ground velocity, PGV). The authors indicated that estimated displacements might be smaller in vector hazard analysis compared to scalar hazard analysis.

Bray and Macedo (2019a, 2019b) expanded the work by Bray and Travararou (2007) considering forward directivity effects; they used a larger set of ground motions comprised of 6,711 two-component horizontal acceleration time histories selected from the NGA-West2 database. They also used a fully coupled, nonlinear, deformable stick-slip model with the modifications by Macedo (2017) and Macedo et al. (2017a). Earthquake-induced slope displacements are estimated from T_s , the spectral acceleration of the ground motion at a degraded period of 1.3 times the fundamental period ($S_{a1.3T_s}$), M_w , and K_y ; in addition, the PGV is also included for near-fault pulse motions.

All the procedures described above have been formulated for shallow crustal earthquakes; the author is aware of only one robust procedure that is developed with a large number of ground motions, considering a variety of slope systems, developed for a different tectonic setting, which corresponds to Bray et al. (2018) model developed for subduction interface earthquakes.

2.1.3 Probabilistic seismic displacement analysis using predictive models

Macedo et al. (2020b, 2020c), Macedo and Candia (2019), Candia et al. (2019a, 2019b), Candia et al. (2018), Macedo et al. (2017b, 2018) have proposed procedures to integrate the predictive models described in the previous section into performance-based probabilistic analyses (*PBPA*), and fully probabilistic performance-based analyses (*FPPBA*). The difference between a *PBPA* and *FPPBA* based analyses is that *FPPBA* considers all *IM* hazard fractiles, whereas *PBPA* considers only the mean. The developments by these authors were integrated into a MATLAB-based platform called *PSDA*, which stands for Probabilistic Slope Displacement Analysis. The platform can be used for *PBPA* and *FPPBA* assessments; it performs *PSHA* and also provides estimates for seismically-induced displacement hazard curves (*DHC*) for systems with contributions from multiple tectonic settings. It considers the epistemic uncertainty in ground-motions and system properties (K_y, T_s) through the logic tree method and polynomial chaos theory (Macedo et al., 2020d). The platform readily provides the *DHCs*, and the process consists of three steps,

1. Estimation of systems properties such as K_y and T_s of the potential sliding mass and the uncertainties in these variables through logic tree method.
2. Perform a site-specific probabilistic seismic hazard analysis to compute S_a hazard curves and deaggregation information at different S_a values.
3. Calculate the seismically induced displacement using the predictive models and construct the displacement hazard curves.

This study will use this platform and compare it with results from advanced numerical simulations.

2.1.4 Estimation of seismically-induced slope displacements using a stick-slip model (Rathje and Bray, 2000)

The seismically-induced deformations can be evaluated by two methods, coupled and decoupled approach. In a decoupled approximation, the estimation of seismic response of the slope structure is separated from the sliding response, i.e., the system's dynamic response is calculated considering it as a flexible system, and the sliding response is evaluated considering it as a rigid structure. In contrast, in a coupled approach, the seismic response and the slope's sliding response are calculated simultaneously (Figure 2-2). Rathje and Bray (2000) formulated a fully coupled nonlinear analytical model for one-directional sliding. In this method, the seismic response of the sliding mass is captured by an equivalent-linear viscoelastic model, which uses strain-dependent material properties. The formulation, models both the forces along the sliding interface and the nonlinear response of the sliding mass; it was also validated against shaking table experiments (Wartman et al., 2003).

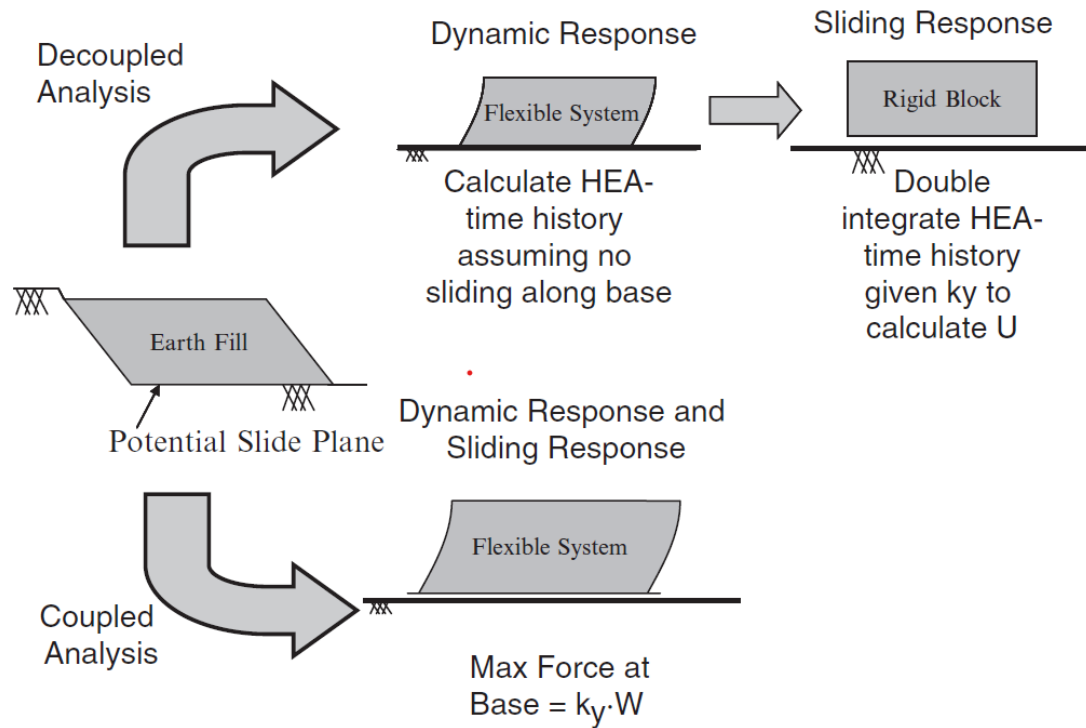


Figure 2-2 Illustration of coupled and decoupled analysis; where *HEA* is the horizontal equivalent acceleration, *U* is the displacement, *W* is the weight of the slope system (Bray, 2007).

2.1.5 Transfer function model (Hale, 2019)

Available analytical procedures utilize only a single proxy ($S_{a1.5T_s}$) or series of proxies (S_a, PGV) to represent the entire ground motion. These analytical procedures rely on functional forms that were developed using large datasets. The transfer function model is an alternative to analytical procedures, and it is based on a decoupled analysis (refer to section 2.1.4), in which the dynamic response of the sliding mass is represented by a transfer function, and the deformations can be calculated by a Newmark-type procedure. Like the stick-slip model, this approach also considers the entire ground motion time

history as opposed to the procedures that rely on predictive equations. Figure 2-3 shows the concept of the transfer function model. The procedure computes a transfer function across all frequencies for the potential sliding mass based on system properties such as height (H), T_s , K_y , which is used to estimate the average acceleration time history for the sliding mass. Using the acceleration time history, deformations can be subsequently calculated using a Newmark-type procedure. The transfer function is based on results from 11,400 dynamic analysis, which included 950 ground motions and 12 representative earthen dams. The dynamic analyses were performed in QUAD4MU (Hudson et al., 2003), which uses the equivalent-linear procedure. The process consists of three steps:

- 1) Computation of the transfer function for the potential sliding mass based on the input system properties.
- 2) Calculation of the average acceleration time history on the sliding mass from the user input ground motion time histories.
- 3) Estimation of shear-induced deformation from the average acceleration time history of the sliding mass using a Newmark-type procedure.

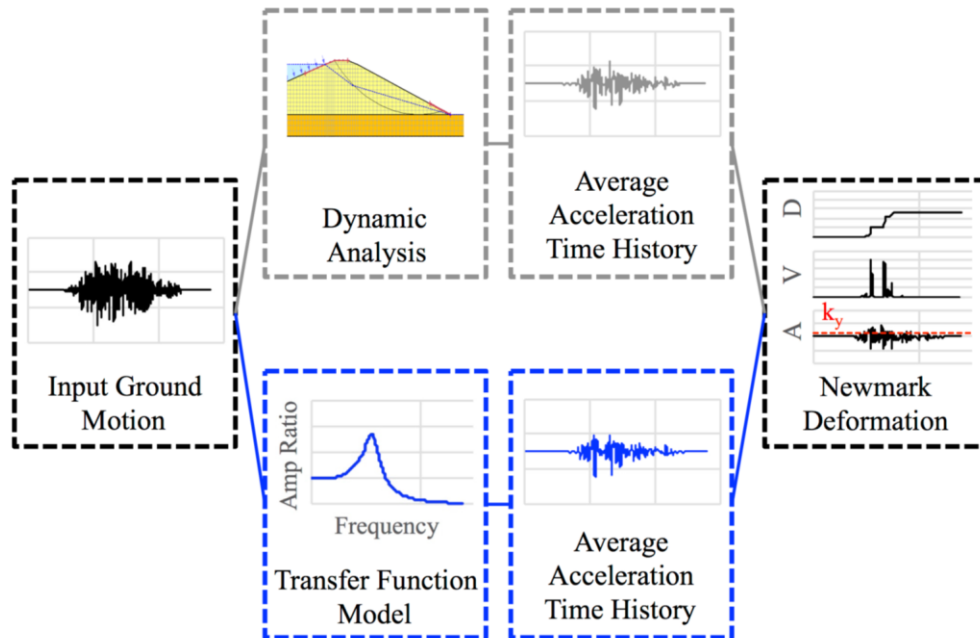


Figure 2-3 Transfer Function Model concept (Hale, 2019).

2.2 Dynamic Response of Rockfill Materials

Rockfill dams are often the most preferred type of dams as, they need less and easier field requirements for foundation, excellent adaptability to geographical and geological conditions, and often have adequate stability against earthquakes (Seo et al., 2009; C. Marulanda and Marulanda, 2015; Bayraktar and Kartal, 2010; Wen et al., 2017). Even though rockfill materials are less prone to liquefaction as there is no excess pore pressure generation, the earthquake-induced deformation could still cause significant damage and needs to be assessed.

Matsumoto (2010) investigated the performance of different types of dams during and after the sequence of shallow crustal earthquakes in Japan. The author inspected five types of

dams (concrete gravity dams, concrete arch dams, earth core rockfill dam, concrete faced rockfill dam, and earth-fill dam) subjected to earthquakes with various magnitude and epicenter distance. He observed that none of the dams suffered any damage when the Japan Meteorological Agency (*JMA*) magnitude is smaller than 6.5. For *JMA* magnitudes greater than 6.5, some dams suffered moderate damage while all concrete dams had no damage. The author also investigated the natural periods, amplification ratio, shear modulus, and PGA attenuation for the five types of dams mentioned above, and the findings are summarized below:

- Natural periods: The natural periods (T) of dams increase with the dam height regardless of the type of dam. For dam structures such as concrete face rockfill dams, the period depends on the ratio of crest length (L) over Height (H), with the relation that T/H decrease as L/H decreases, which indicates that the natural period of this type of dams is affected by abutment constraint.
- Amplification ratio: The amplification ratio of *PGA* from the dam foundation to its crest decreases with foundation *PGA*'s increase due to the nonlinear behavior of the material. The amplification ratios for rockfill and earth-fill dams are much lower than concrete dams, which indicates that the fill dams exhibit a larger damping ratio than concrete dams.
- Shear modulus: The shear modulus decreases as the shear strain increases. For rockfill dams subjected to severe earthquake loading, the shear modulus decreases significantly to $1/10$ of maximum shear modulus (G_{max}).

- *PGA* attenuation: The *PGA* at the soil surface, below the soil surface, and dam foundation were compared and was found that *PGA* at the soil surface is much higher than *PGA* at the underlying dam foundation.

Park and Kishida (2019) studied the seismic response of embankment dams based on recorded strong motion data in Japan. They analyzed the correlation between dam's dynamic responses and ground motion parameters. The authors found that for *PGA* in the foundation greater than 0.2g, the amplification factor decreases as *PGA* increases. They studied the variation of seismic response of dams with the dam geometry (e.g., dam height, length) and observed that the fundamental period increases as height (H), length (L), and *PGA* increases. They used multiple linear regression models to predict the fundamental period based on height, length, and *PGA* for embankment dams. Finally, they proposed models to estimate the fundamental period as a function of input motion and geometry (H , L).

Li et al. (2008) studied a 240 m tall core-rockfill dam and presented shear modulus reduction curves obtained in the range of confining pressure of 300 to 2500 kPa in the range of 0.0001 to 1 % of shear deformation. They noticed, from the laboratory tests that, as the confinement stress increases, the material behaves more linear.

Zhou et al. (2016) conducted a study using a large-scale triaxial test to test rockfill materials. They found that the small-strain shear modulus of rockfill materials is affected mainly by the confining pressure, the void ratio, and the initial stress ratio. The experimental results exhibit that the small-strain shear modulus decreases with increasing void ratio and increases with increasing confining pressure and initial stress ratio. The results also revealed a considerable decrease of damping ratio with increasing confining

pressure, which is consistent with the report by Li et al. (2008). In addition, they compared their results with those obtained by Rollins et al. (1998) and found it to be consistent. Finally, they developed expressions to estimate the shear modulus reduction curves for rockfill materials.

Kishida et al. (2019) reviewed 27 downhole recordings at nine embankment dams in Japan from 1987 to 2011 to study the dynamic properties of core materials. The apparent shear strain was computed from the difference in displacement time series and the separation distance between sensors. It was found that the apparent shear wave velocity (V_s) decreased, and the shear strain increased when the strong shaking propagated. The recordings were rotated for different azimuthal angle to study the orientation-dependent characteristics of V_s and shear strains (γ) and it was observed that V_s did not change much with different azimuthal angles, whereas γ ranged widely depending on the azimuthal angles. The in-situ G/G_{max} and G were calculated using the recorded V_s and assumed unit weight. These values were compared with data from empirical models from previous studies. They found that the in-situ G/G_{max} data range widely depending on the dam, and hence the best-fitting empirical model varies for each dam. The authors also observed large uncertainties in the in-situ G/G_{max} data. Based on conditional probability, a methodology was developed to update the in-situ modulus reduction curve by considering the observed data and their measurement uncertainties.

Zhu et al. (2014) carried out laboratory experiments and investigated the dynamic property of gravels under high confining pressure to simulate rockfill dams with heights greater than 200m. The authors state that previous studies were based on a relatively low confining pressure (10 to 500 kPa), which does not properly describe the behavior of dams as the

stress from high dams can be as high as 3000 kPa. In their study, 42 large cyclic triaxial tests (*CTX*) were carried out on 12 gravel samples with confining pressures ranging from 227 to 4000 kPa. Since the maximum diameter of the gravels exceeds the capacity of a typical large-scale *CTX*, Zhu et al. (2014) developed a special approach to handle oversized gravel particles. Their results are summarized below:

- Shear modulus reduction: The modulus reduction curve, $G/G_{max} - \gamma$, is shifting upward as the confining pressure increases, indicating increased shear modulus. However, these modulus reduction curves fall within the range of the curves recommended by Seed et al. (1986) for lower confining pressure. This is due to the higher loading frequency used in this study. The high loading frequency will shift downward the reduction curve, counteracting the upward shift caused by high confining pressure.
- Damping ratio: The damping ratio curve, shifts downward as the confining pressure increases, indicating reduced damping. Similarly, all the damping curves fall within the range of curves recommended by Seed et al. (1986). This is also because, the high loading frequency shifts the damping curves upwards.

Figure 2-4 presents the shear modulus reduction and damping curves for rockfill materials compiled from the available literature. These curves are used later in this study for calibrating the constitutive models.

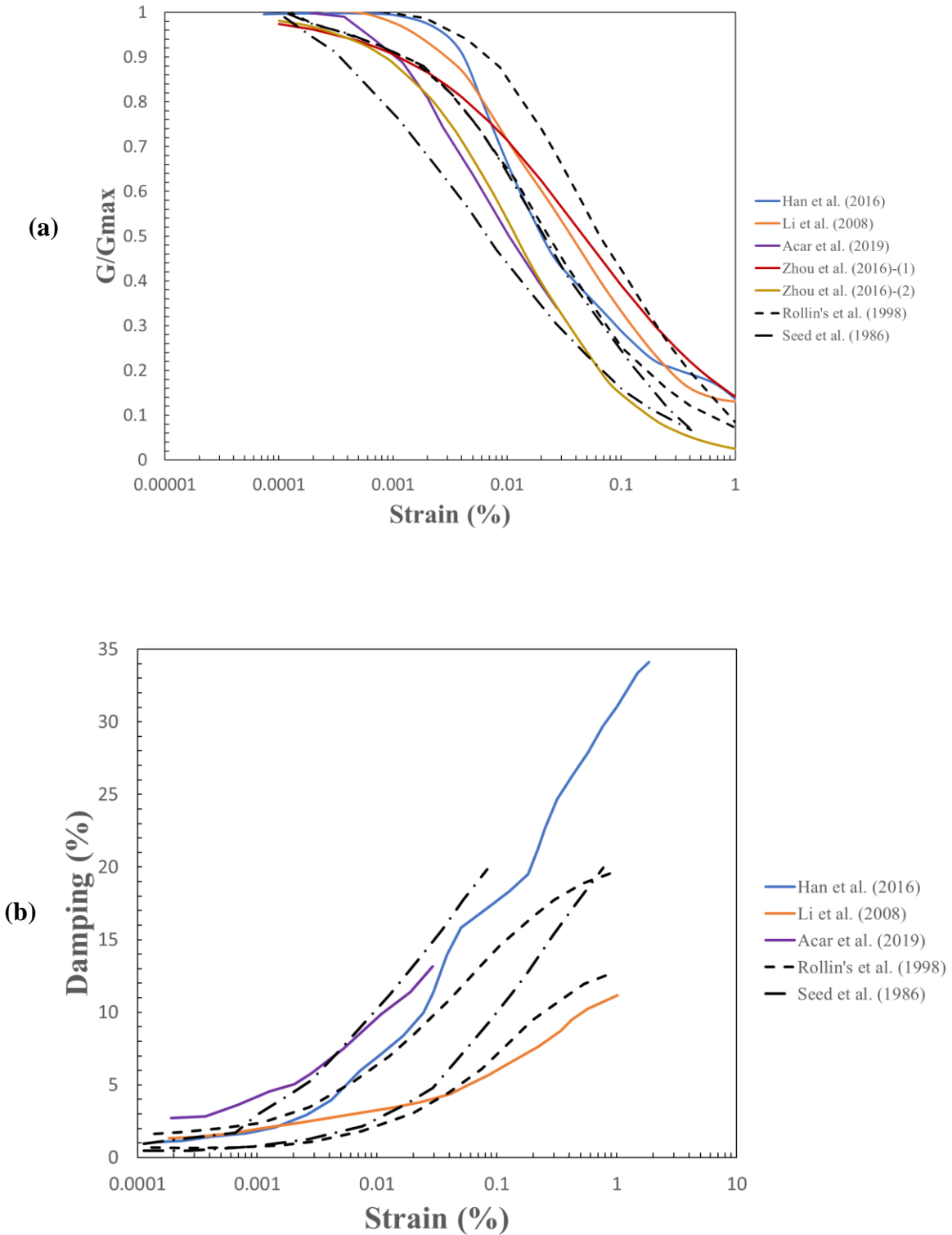


Figure 2-4 (a) Shear modulus reduction curves compiled from the literature (b) Damping curves obtained from the literature

CHAPTER 3. SELECTION OF GROUND MOTION TIME HISTORIES

3.1 Probabilistic Seismic Hazard Analysis

The selection of input time histories is a vital step to perform dynamic analyses of a rockfill dam. To select ground motions, the preliminary step is to perform a site-specific probabilistic seismic hazard analysis (*PSHA*). Seismic hazard associated with a site, influenced by N sources can be computed using the expression,

$$v(S_a(T) > z) = \sum_{i=1}^{N_{Source}} \sum_{j=1}^{N_{Scenario}} \left(rate_j((M, R)_j, Source_i) \right) * P(S_a(T) > z | (M, R)_j) \quad (1)$$

where, $v(S_a(T) > z)$ is the annual rate of exceedance for a spectral acceleration threshold z , at a given period T , M is the earthquake magnitude, R is the site to source distance, $rate_j((M, R)_j, Source_i)$ corresponds to the rate of occurrence of a particular earthquake scenario, $P(S_a(T) > z | (M, R)_j)$ is the conditional probability that the spectral acceleration at a given period ($S_{a(T)}$) will exceed the threshold S_a value (z) for a given M and R . Figure 3-1 describes the four major steps involved in *PSHA*, which are 1) Identification and characterization of earthquake sources at the site, 2) Characterization of seismicity of each source and estimation of the rate of occurrence of each scenario, 3) Estimation of ground motion intensity measure produced at the site by any possible earthquake scenario, 4) Computation of the annual rate of exceedance of a ground motion parameter by combining results from all scenarios and ground motions using Equation 1.

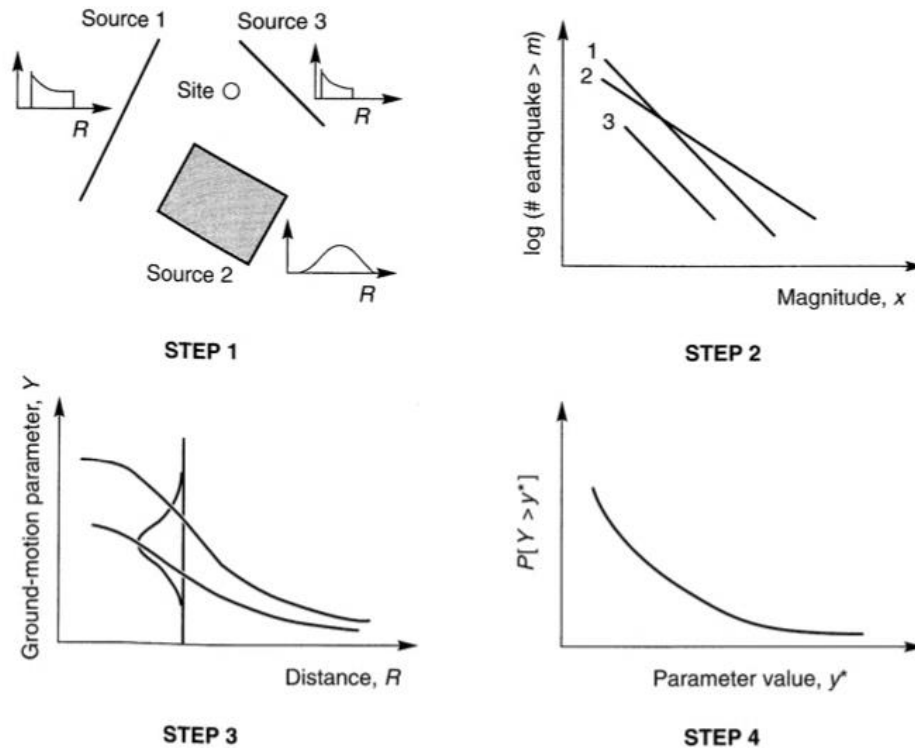


Figure 3-1 Four steps involved in a probabilistic seismic hazard analysis (Kramer, 1996)

In this study, the *PSHA* for the selected site is performed using the platform *HAZ45* (Abrahamson, 2017). The selected dam is situated in a highly seismic shallow crustal region located in California with potential seismic hazard from 159 faults (within 400 km from the site). An average shear wave velocity of 760 m/s for the upper 30 meters was used. Hazard curves for spectral acceleration are calculated using Equation 1 and ground motion prediction equations (Abrahamson et al., 2014; Boore et al., 2014; Campbell and Bozorgnia, 2014; Idriss, 2014). Then, uniform hazard spectra (*UHS*) are constructed from the hazard curves. A total of 10 *UHS* are constructed over hazard levels ranging from 1.00 E-2 to 1.00 E-7, dividing them into ten equal parts in log scale. As discussed later, it is important to construct *UHS* over a wide range, as it will be used to reproduce hazard over

the site. The hazard curves for PGA, S_a at different periods are shown in Figure 3-2, and the *UHS* for hazard levels from $1.00 \text{ E-}2$ to $1.00 \text{ E-}7$ are presented in Figure 3-3.

The *PSHA* results have been used to perform deaggregation analyses, which identify the fractional contribution from different earthquake scenarios, dictated by combinations of M and R to the total hazard. Figure 3-4 shows the contribution of (M, R) pairs to the total hazard for a spectral period of 0.5 seconds and for a return period of 100 years. For the selected site, at a period of 0.5 seconds, the contribution to the lowest hazard level of $1.00 \text{ E} - 2$, corresponding to a return period of 100 years is controlled by a mean earthquake magnitude of 6.51 with a mean distance of 68 km and the contribution to the highest hazard level of $1.00 \text{ E} - 7$, corresponding to a return period of 10,000,000 years is controlled by a mean earthquake magnitude of 6.4 with a mean distance of 12.4 km. Table 1 shows the mean magnitude and distance for all selected hazard levels for a period of 0.5 seconds.

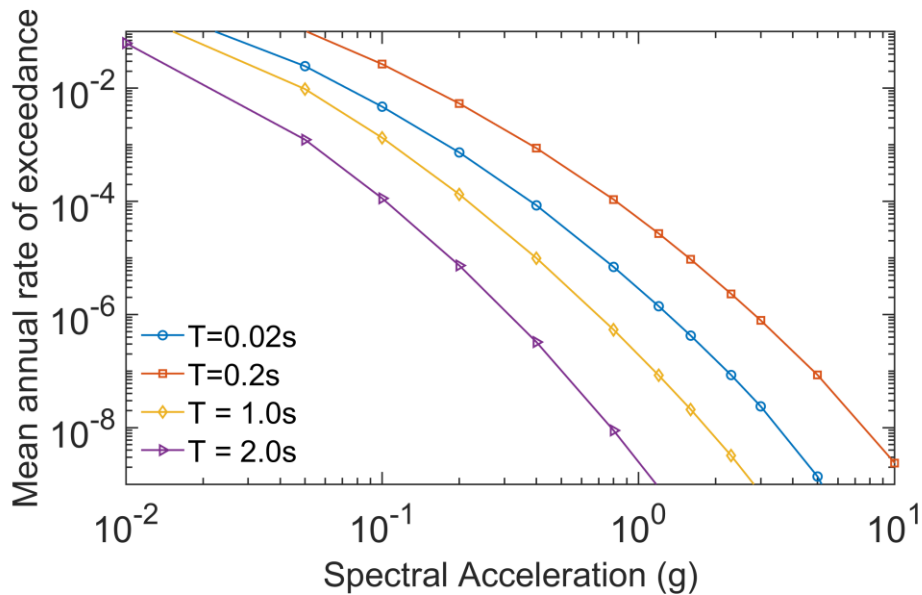


Figure 3-2 Mean hazard curves obtained from PSHA

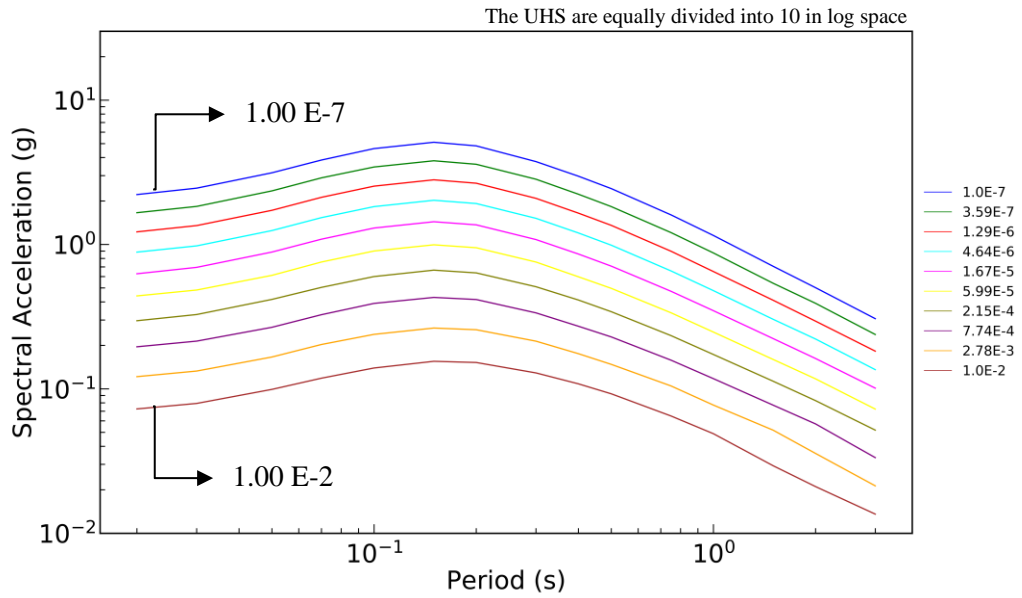


Figure 3-3 Uniform hazard spectrum obtained from PSHA

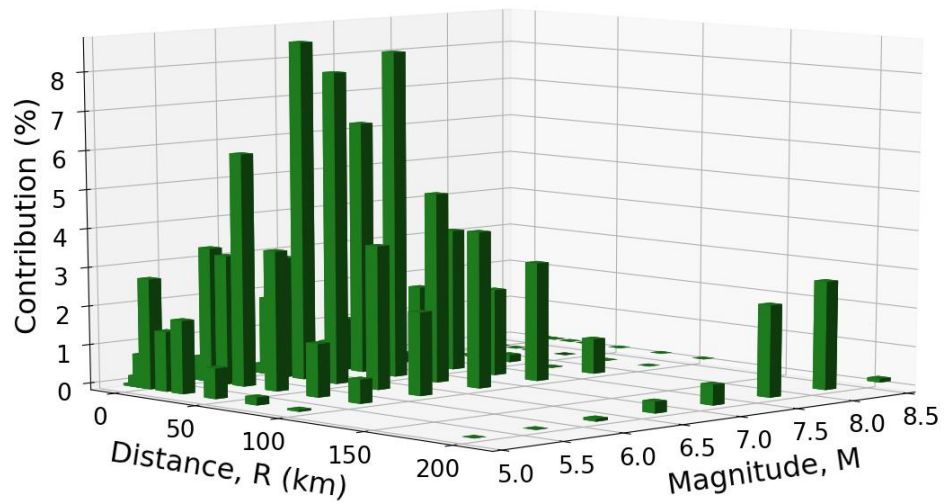


Figure 3-4 Deaggregation of the seismic hazard at the selected site for spectral period of 0.5 seconds for a return period of 100 years

Table 1 - Mean magnitude and distance contributing to all selected hazard levels for a period of 0.5 seconds obtained from hazard deaggregation

Hazard	Mean Magnitude	Mean Distance (km)
1.00 E-2	6.51	68.0
2.78 E-3	6.51	68.0
7.74 E-4	6.49	49.6
2.15 E-4	6.46	34.2
5.99 E-5	6.46	34.2
1.67 E-5	6.44	23.3
4.64 E-6	6.44	23.3
1.29 E-6	6.42	18.2
3.57 E-7	6.41	15.2
1.00 E-7	6.40	12.4

3.2 Ground-motion Database

A subset of the NGA-West2 database developed by PEER (Ancheta et al., 2014) was used in this study. The subset was selected considering earthquake magnitude above five and rupture distance in the range of 0 to 300 km. The selected subset contains a total of 2649 earthquake recordings, each with three components (two horizontal and one vertical) hence giving a total of 7947 recorded time histories. Figure 3-5 shows the distribution of magnitude and rupture distance in the selected database, Figure 3-6 to 3-8 shows the distribution of *PGA*, arias intensity, V_{S30} in the selected subset.

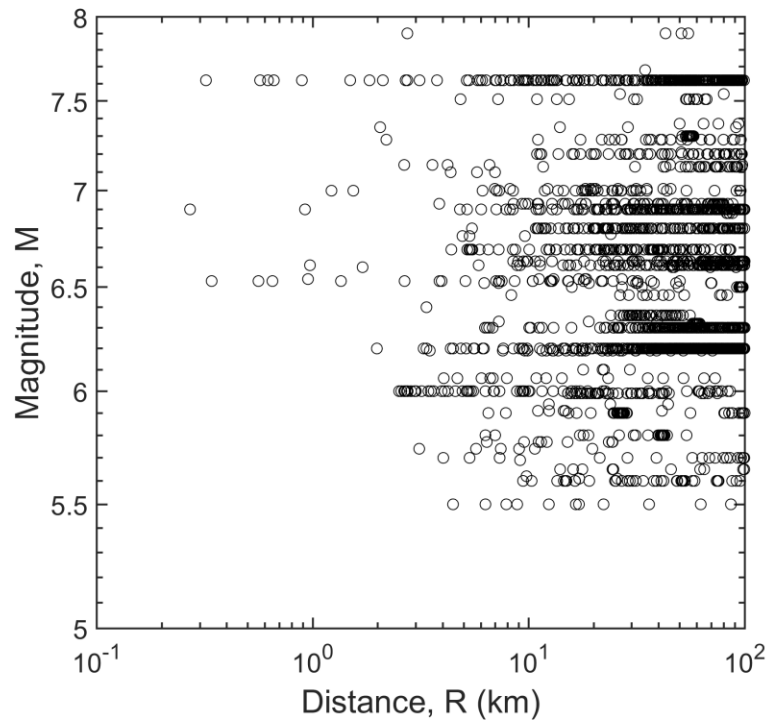


Figure 3-5 Magnitude-distance distribution of the selected subset

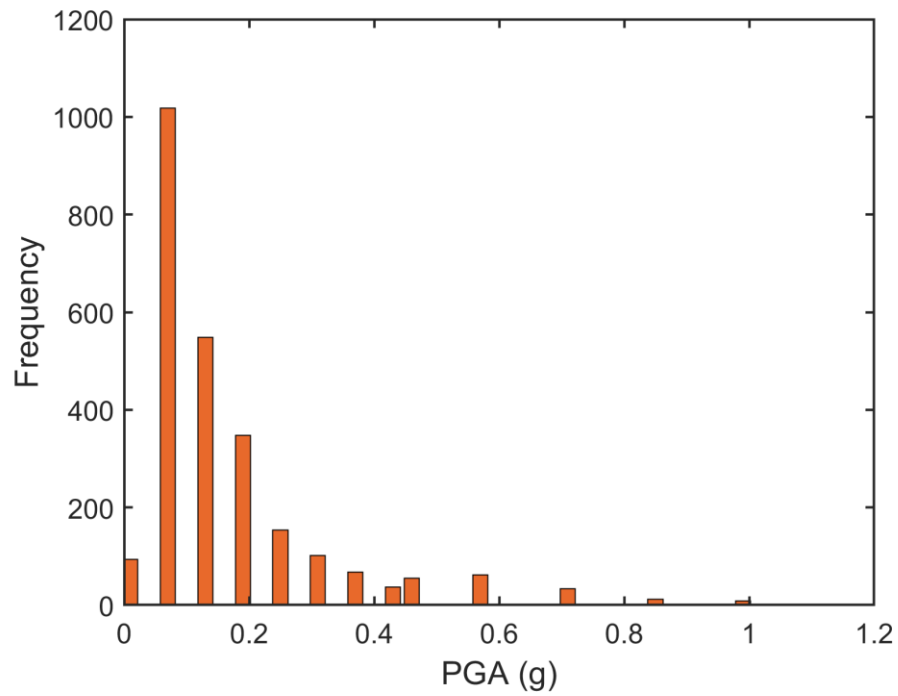


Figure 3-6 Distribution of PGA in the selected subset

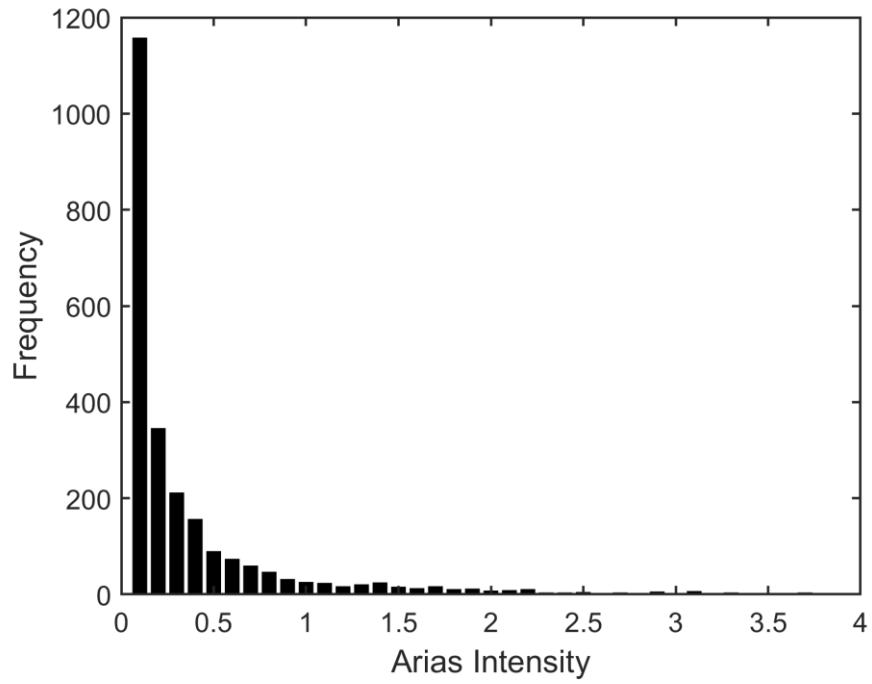


Figure 3-7 Distribution of Arias Intensity in the selected subset

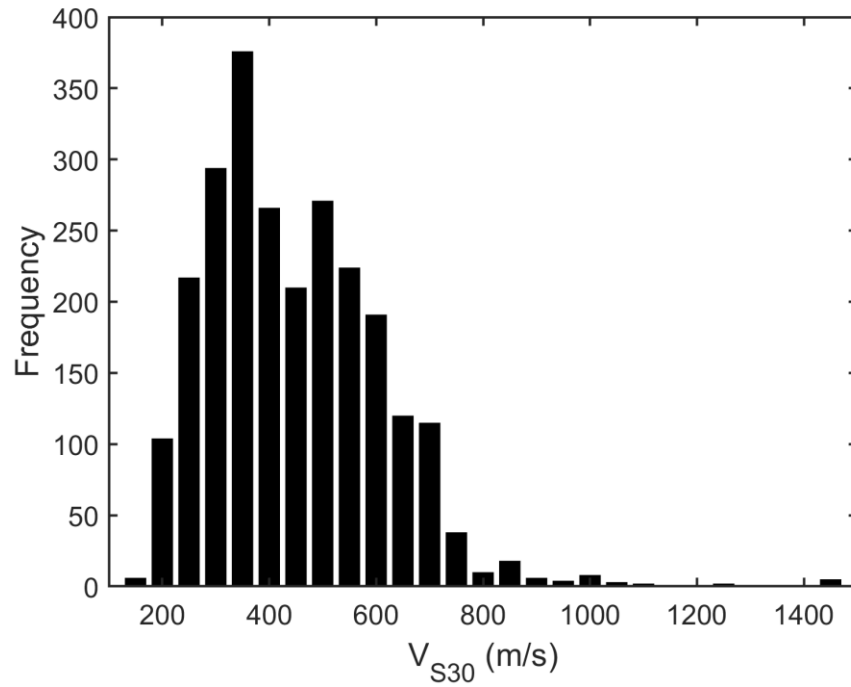


Figure 3-8 Distribution of V_{S30} in the selected subset

3.3 Conditional Scenario Spectra

This study used the conditional scenario spectra (*CSS*) framework to select the ground motions used in the subsequent time history dynamic analysis. The *CSS* framework considers a set of ground motion time histories, each with an assigned rate of occurrence, that reproduces hazard over a site (Arteta and Abrahamson, 2018). Each ground motion time history selected using *CSS* comes with a rate of occurrence that can be used to develop *EDP* hazard curves. *CSS* includes the following steps:

- 1) The first step to develop *CSS* is to construct the conditional mean spectrum (*CMS*) (Baker, 2011) for all selected design hazard levels. The *CMS* is developed using the mean magnitude and distance obtained from deaggregation for a conditioning period of 0.5 seconds. Therefore, a total of 10 *CMS* were computed for hazard levels from $1.00 E - 2$ to $1.00 E - 7$. Figure 3-9 shows the *CMS* constructed over *UHS* of all hazard levels. The mean response spectrum, epsilon and correlation coefficient at each period was calculated using Baker and Jayaram (2008). The *CMS* variability (+/- 2.5) is also calculated using Jayaram et al. (2011) using:

$$\sigma_{\ln Sa(T_i) | \ln Sa(T^*)} = \sigma_{\ln Sa(T_i)} \sqrt{1 - \rho^2(T_i, T^*)} \quad (2)$$

where $\sigma_{\ln S_a(T_i)}$ is the standard deviation in $\ln S_a(T_i)$, $\rho(T_i, T^*)$ is the correlation coefficient.

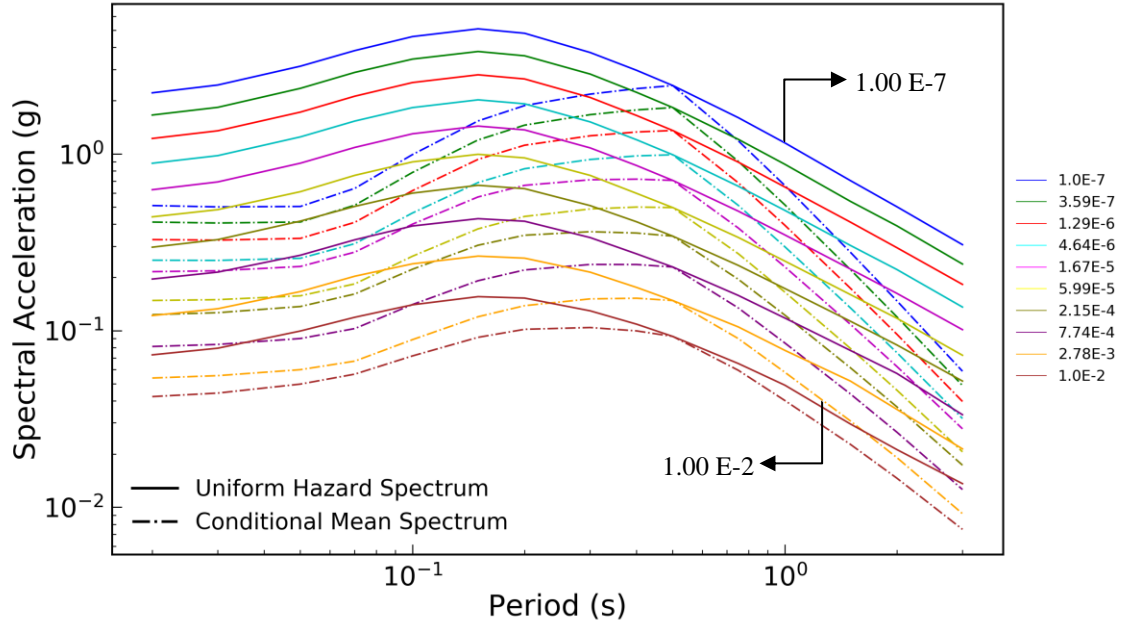


Figure 3-9 Conditional mean spectra constructed for all selected hazard levels.

- 2) The second step is to select a set of time histories from the suite of ground motions and scale it to match *CMS* and its variability (± 2.5) for each hazard level of interest. For each hazard level, a set of N ground motions that best represent *CMS* and its variability were selected from the subset using Monte Carlo simulations. The log-likelihood for selecting this N time histories for hazard level k is given by,

$$LL_k = \sum_{j=1}^{nPer} \sum_{i=1}^N -\ln(\sigma_{CMS,T_0}(Z_k, T_j)) - \frac{(\ln(\alpha_{ik} S_{a,i}(T_j)) - \ln(S_{a,CMS,T_0}(Z_k, T_j)))^2}{2\sigma_{CMS,T_0}^2(Z_k, T_j)} \quad (3)$$

where α_{ik} is the scaling factor applied to i^{th} time history for the k^{th} hazard level. The set with the best fit to the *CMS* and its variability, i.e., the set with maximum likelihood, is

selected and is the CSS for that hazard level. Figure 3-10 shows the CSS selected for a hazard level of $1.00 E - 2$ ($N=32$).

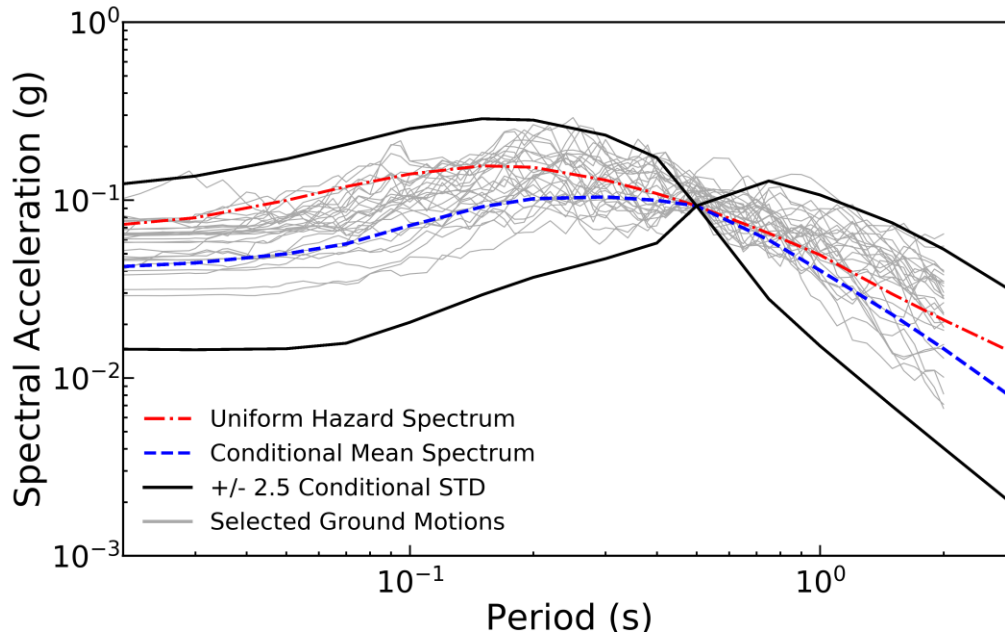


Figure 3-10 Set of time histories selected and scaled based on CMS and its variability for a hazard level of $1.00E - 2$

- 3) The next step is to assign the rate of occurrence to each selected time history. The initial rate of occurrence of each time history is computed from the neighboring hazard levels. It is calculated by,

$$Rate_{CSS0,i} = \frac{HazLev_i - HazLev_{i+1}}{N} \quad (4)$$

where $Rate_{CSS0,i}$ is the initial rate assigned by CSS to the time history at i^{th} hazard level, $HazLev_i$ is the hazard level (i) and $HazLev_{i+1}$ is the hazard level ($i+1$).

- 4) The final step is to reconstruct the hazard curves using the selected scaled subset of time histories and their corresponding rate of occurrences using the equation,

$$v(S_{a(T)} > z) = \sum_{i=1}^{\# \text{ recordings}} Rate_{CSS,i} H(\alpha_i S_{a,i}(T) - Z) \quad (5)$$

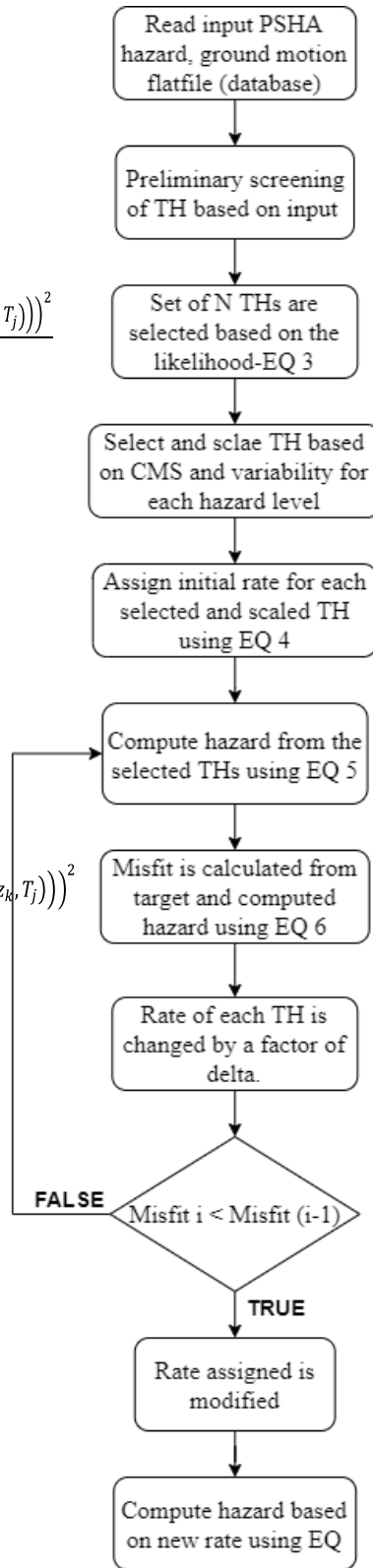
where $S_{a,i}$ is the spectral acceleration of the i^{th} recording, α_i is the scale factor, and H is the Heaviside function, which is either one or zero. The rate of occurrence of each time history is then adjusted using a penalty function to better reproduce the hazard. This function is iterated until a minimum value for the penalty function is obtained.

$$Penalty = \sum_{j=1}^{nPer} \sum_{k=1}^{nHaz} wt(T_i) \left(\ln \left(HAZ_{CSS}(z_k, T_j) \right) - \ln \left(HAZ_{PSHA}(z_k, T_j) \right) \right)^2 \quad (6)$$

where $wt(T_i)$ is the weight assigned for a given period, HAZ_{PSHA} is the hazard computed from *PSHA* and HAZ_{CSS} is the hazard recovered from *CSS*. Figure 3-11 shows a flow chart that illustrates the different steps involved in the process of computing *CSS*.

$$LL_k = \sum_{j=1}^{nPer} \sum_{i=1}^N -\ln(\sigma_{CMS,T_0}(z_k, T_j)) - \frac{(\ln(\alpha_{ik} S_{a,i}(T_j)) - \ln(S_{a,CMS,T_0}(z_k, T_j)))^2}{2\sigma_{CMS,T_0}^2(z_k, T_j)}$$

$$Penalty = \sum_{j=1}^{nPer} \sum_{k=1}^{nHaz} wt(T_i) (\ln(HAZ_{CSS}(z_k, T_j)) - \ln(HAZ_{PSHA}(z_k, T_j)))^2$$



$$Rate_{CSS0,i} = \frac{HazLev_i - HazLev_{i=1}}{N}$$

$$Sa_{haz1(iPer,iLev)} = Sa_{haz(iPer,iLev)} \pm Rate_i * delta$$

Figure 3-11 Flow chart illustrating the steps involved in CSS.

Figure 3-12 shows the target hazard obtained from *PSHA*, initial hazard computed from *CSS* and final hazard recovered from *CSS* after applying the penalty function for a spectral period of 0.5 seconds.

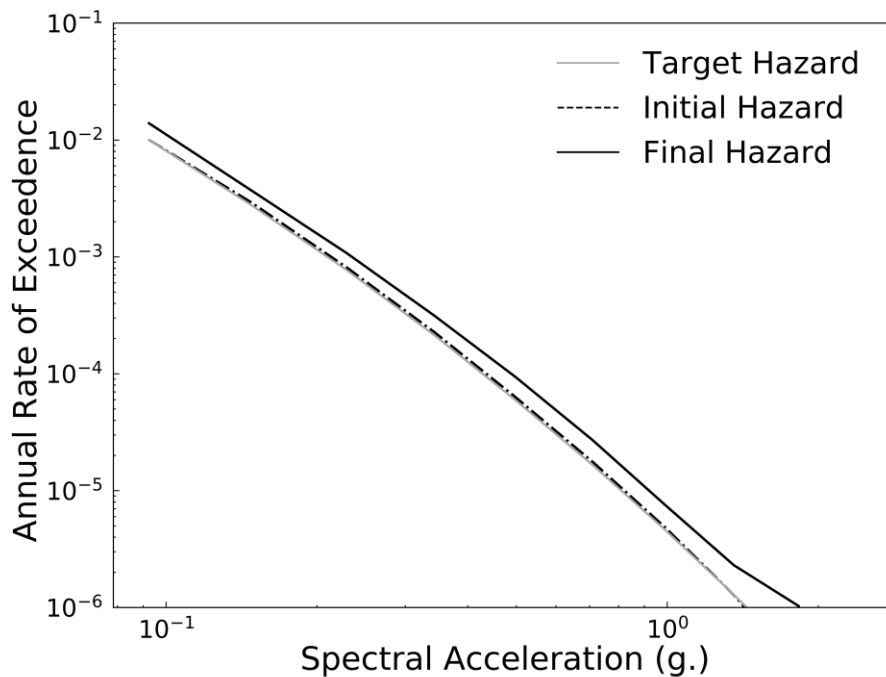


Figure 3-12 Hazard curve recovered from CSS for a spectral period of 0.5 seconds.

3.4 Selected Scenario Spectra

Using the procedures described in the previous sections, a set of 60 unique single component ground motions were selected; some of these were scaled to different hazard levels and assigned different rates of occurrences, making a total of 220 scaled ground motions to reproduce hazard over different hazard levels over the site. Figure 3-13 shows the distribution of magnitudes and rupture distances for the selected ground motions. Figure 3-14 presents the distribution of *PGA* for the selected ground motions. Figure 3-15

shows the selected ground-motion spectra, and Figure 3-16 shows the assigned rate of occurrence for each spectrum of the *CSS*. Figure 3-17 presents the *UHS* reconstructed through the *CSS* approach and the target *UHS* obtained from *PSHA*. It can be seen that the *UHS* recovered from *CSS* matches reasonably with that from *PSHA*.

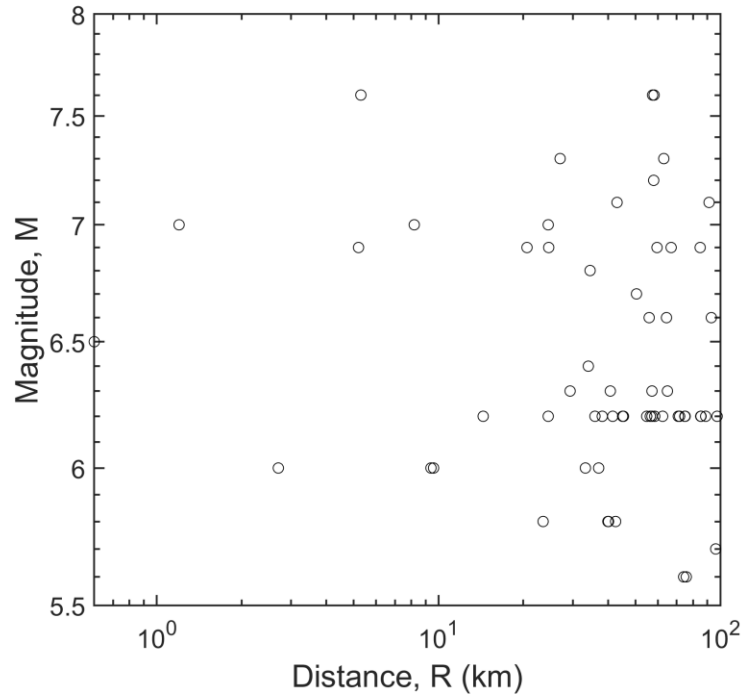


Figure 3-13 Magnitude-distance distribution for the selected ground motions

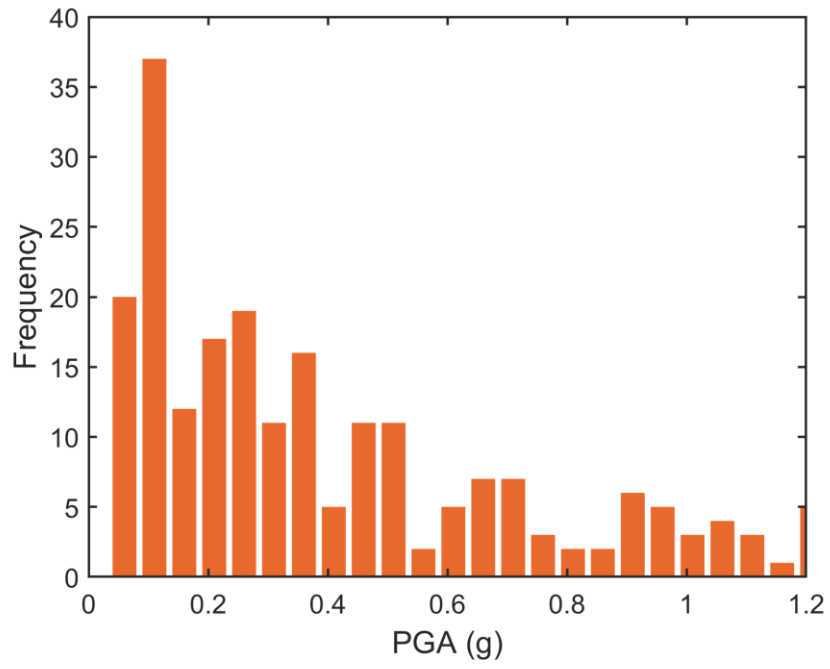


Figure 3-14 Distribution of PGA for the selected ground motions

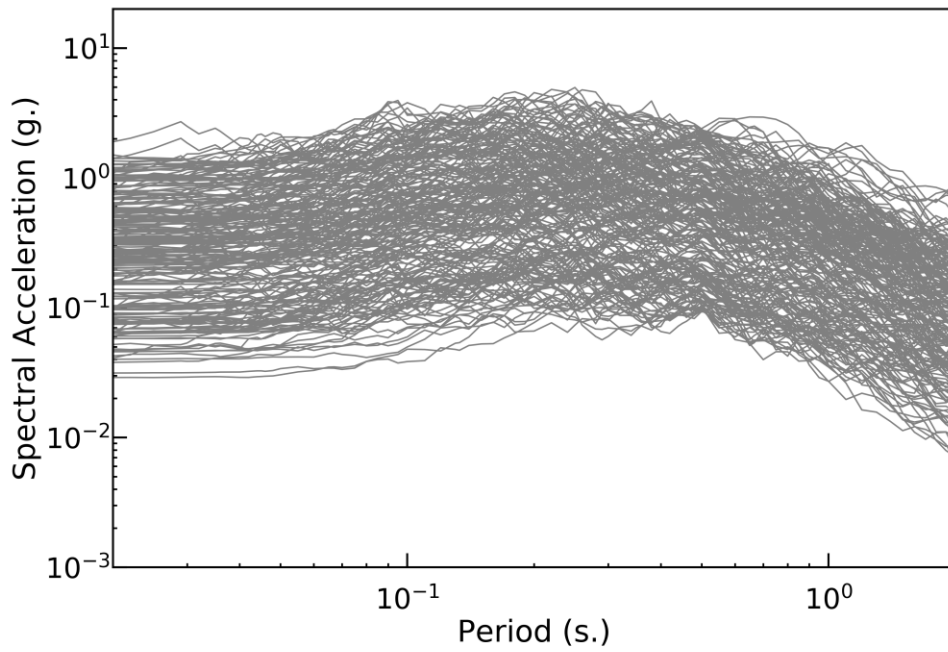


Figure 3-15 All selected scenario spectra from CSS

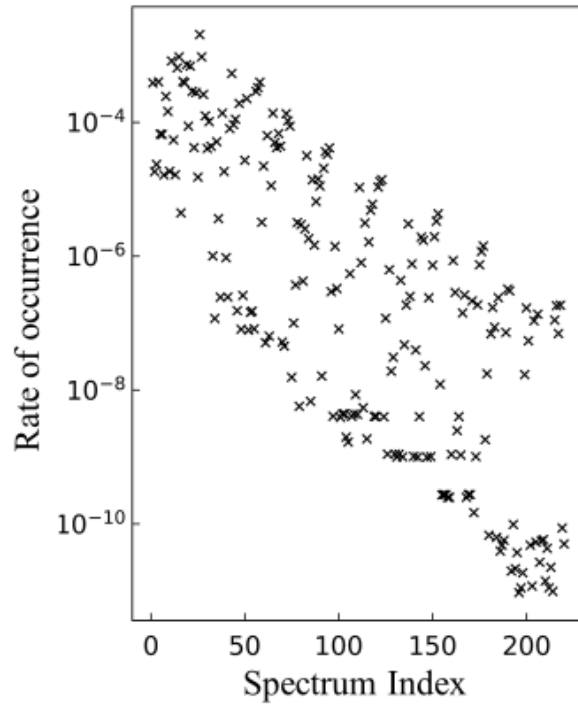


Figure 3-16 Final rate of occurrence for each spectrum

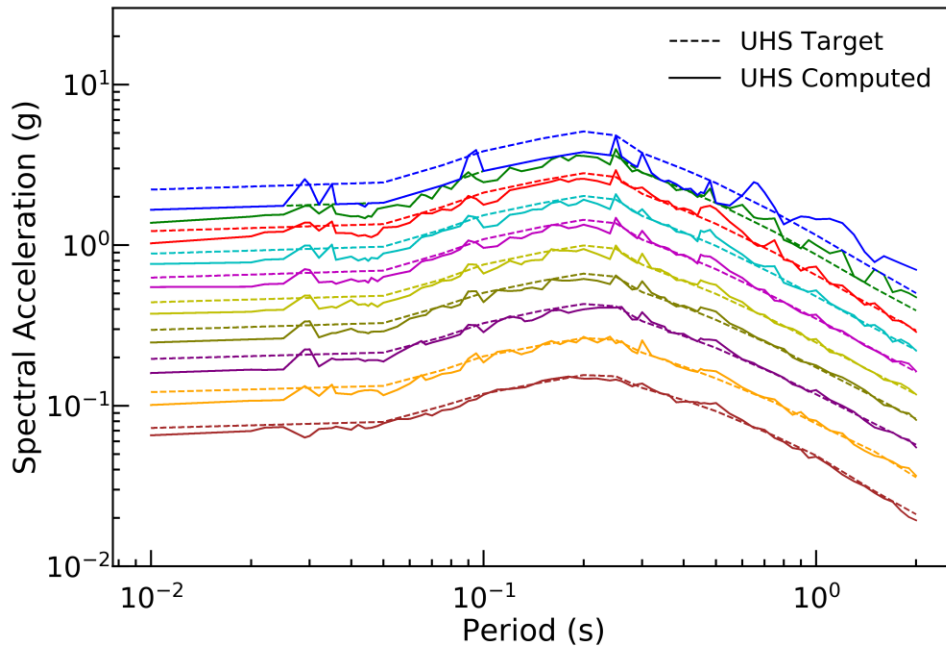


Figure 3-17 Comparison of target uniform hazard spectrum from PSHA and uniform hazard spectrum recovered from CSS.

CHAPTER 4. PERFORMANCE-BASED SEISMIC ASSESSMENT USING ANALYTICAL METHODS

4.1 Evaluation of Seismic Yield Coefficient

The critical components for seismic displacement analysis are a) Dynamic resistance of the slope system, b) Earthquake ground motion, c) System's flexibility. The dynamic resistance of a slope system is represented by K_y , which is the pseudo-static seismic coefficient when the factor of safety is equal to 1.0. When the input earthquake acceleration exceeds this K_y , displacement occurs. A lower K_y corresponds to lower dynamic resistance, which will lead to higher displacements and vice versa. The earthquake ground motion is represented through IMs , and the system's flexibility is represented by the initial fundamental period.

The dam structure considered in this study is a 44-meter tall rockfill dam with a downstream slope of 1:1.3. The dam structure is divided into three different layers based on type of materials, 1) Rockfill 2) Streambed gravel 3) Bedrock, as shown in Figure 4-1. The K_y for the dam structure used is evaluated using the limit equilibrium computer program SLIDE (Rocscience, 2018). The material properties used for each layer for this analysis are shown in Table 2.

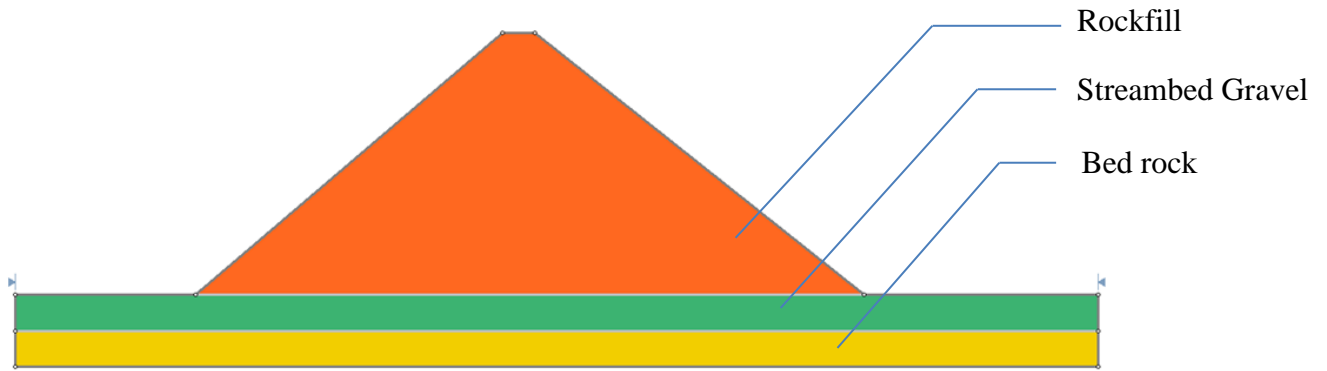


Figure 4-1 Geometry of the dam and different layers.

Table 2- Material properties used for different layers for analysis in SLIDE.

Material	Friction angle (°)	Unit weight (kN/m^3)	Cohesion (kPa)
Bedrock	45	22	250
Streambed Gravel	42	15	0
RockFill	45	19	0

A range of K_y values, varying from 0.12 to 0.2, for a range of slip surfaces were computed.

The slip surfaces for K_y values 0.12, 0.15, 0.2 are shown in the Figures 4-2 to 4-4. It can be seen that the sliding mass increases as the K_y value increases; this is because the system shows higher resistance to displace higher mass.

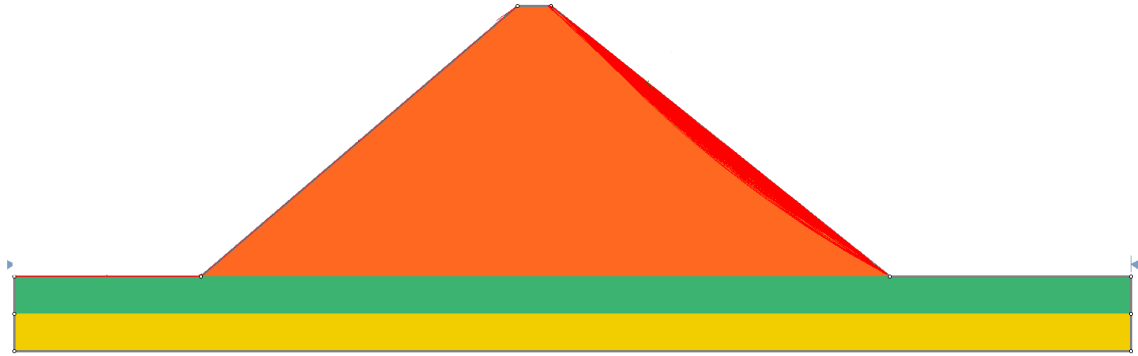


Figure 4-2 Slip Surfaces for yield coefficient value of 0.12.

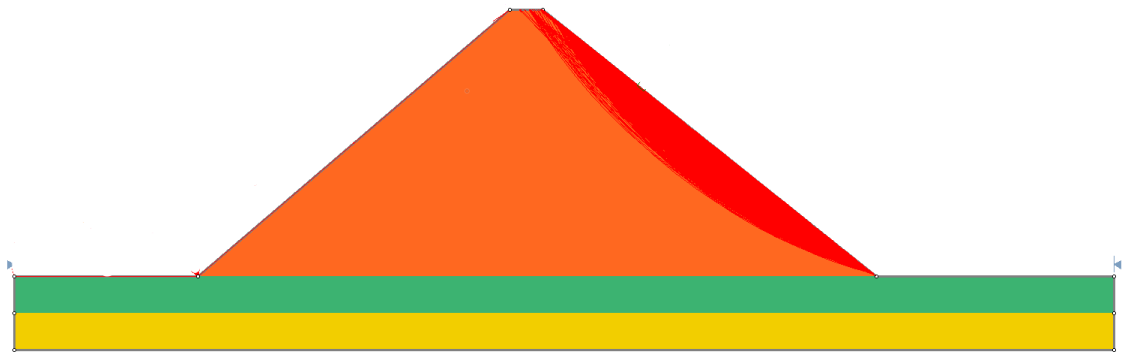


Figure 4-3 Slip Surfaces for yield coefficient value 0.15.

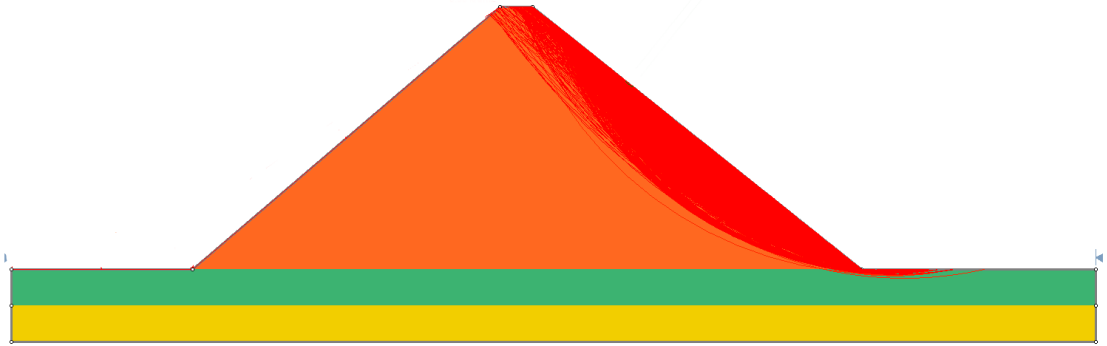


Figure 4-4 Slip Surfaces for yield coefficient value 0.2.

4.2 Probabilistic Seismic Displacement Analysis (PSDA)

As detailed in Section 2.1.3, *PSDA2* is an integrated platform with a graphical user interface (*GUI*) to perform performance-based probabilistic analyses (*PBPA*). For this study, we only considered the mean hazard curve obtained from *PSHA* and not the full set of fractiles. To consider the epistemic uncertainty associated with the system properties, a logic tree considering five branches for K_y with a coefficient of variation of 0.2 is used. Each branch is assigned a specific weight. The model's epistemic uncertainty was also taken into account by considering two different models, namely Bray and Macedo (2019) (BM2019) and Bray and Travarasrou (2007) (BT2007), each with an equal weight of 0.5. A fundamental period of 0.2 seconds was used for the calculations. Figure 4-5 illustrates the logic trees with the weights used. *PSDA2* outputs the displacement hazard curves calculated from each branch along with the weighted mean hazard curve. Figures 4-6 to 4-

8 shows the displacement hazard curves obtained from *PSDA2* for three different mean K_y values.

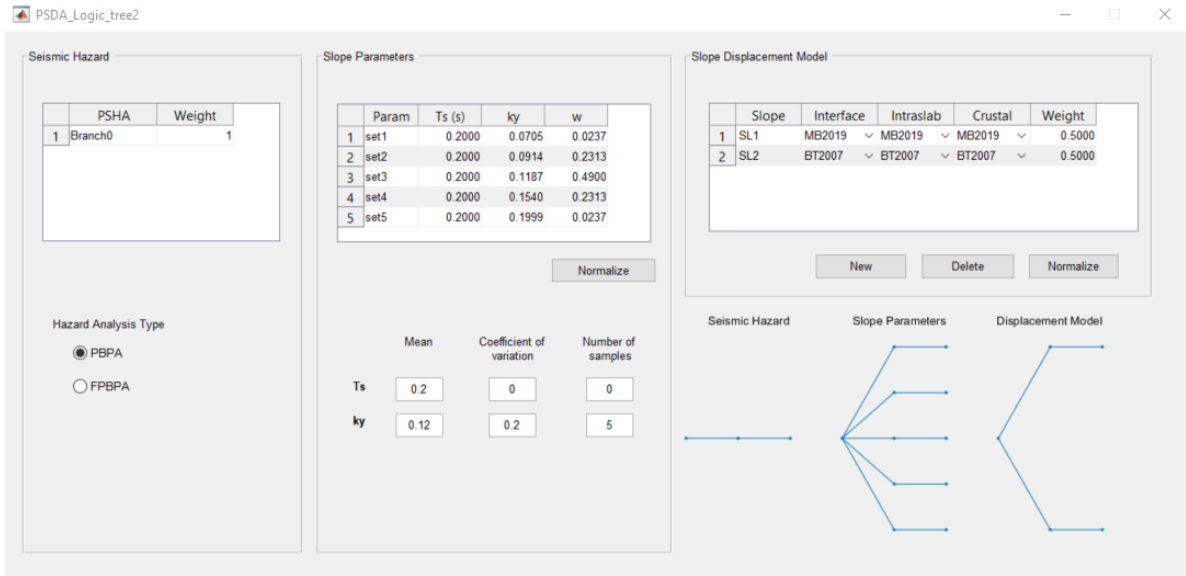


Figure 4-5 Snapshot from PSDA2 platform showing different branches and weights for a mean K_y value of 0.12.

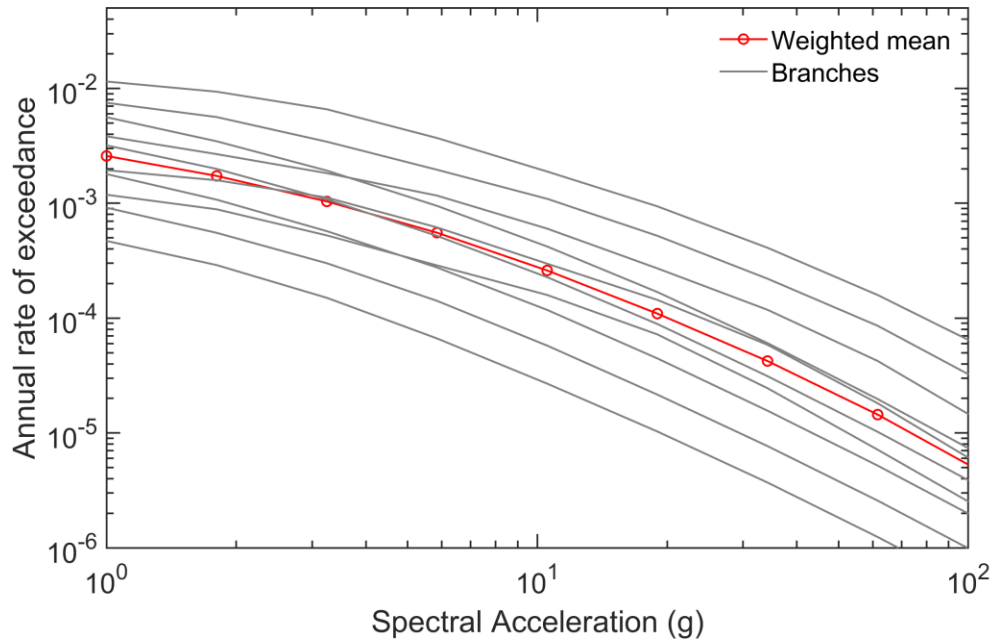


Figure 4-6 All fractiles of displacement hazard curves and weighted mean obtained from PSDA2 for a mean K_y value of 0.12.

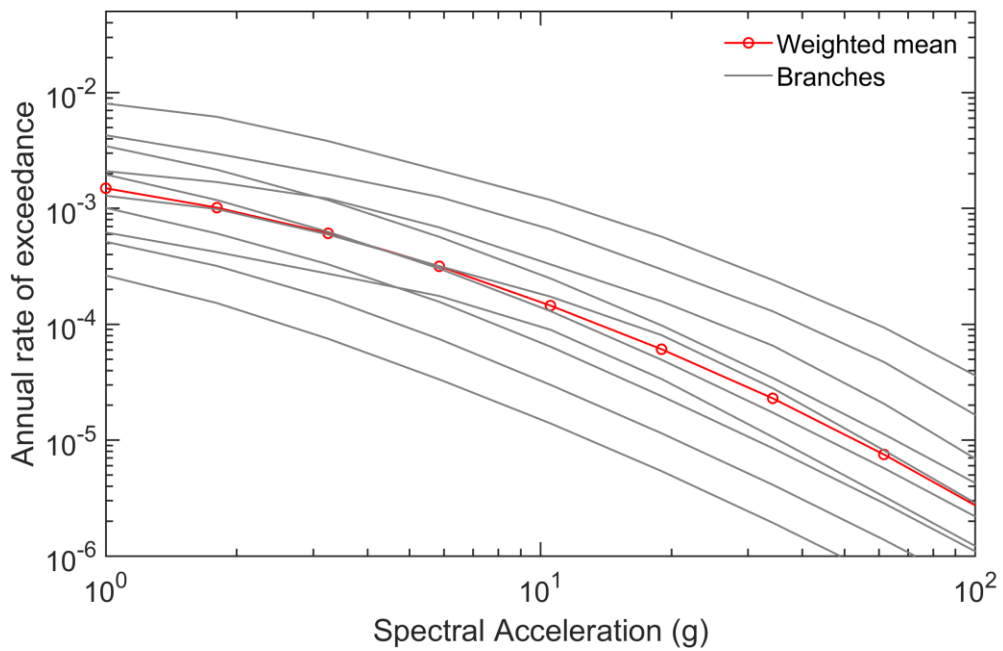


Figure 4-7 All fractiles of displacement hazard curves and weighted mean obtained from PSDA2 for a mean value K_y of 0.15.

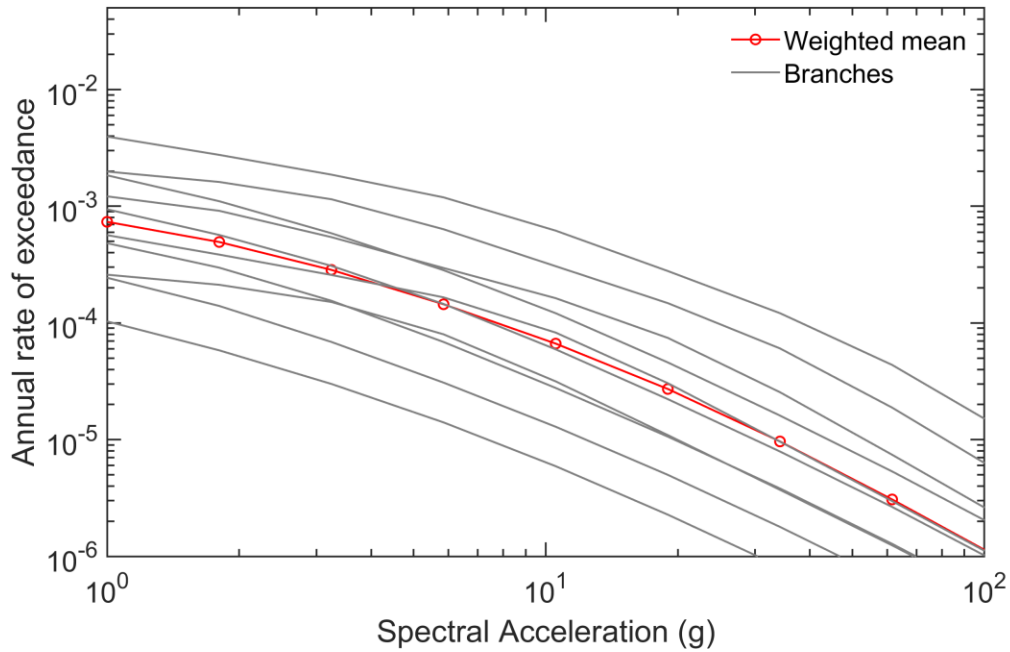


Figure 4-8 All fractiles of displacement hazard curves and weighted mean obtained from PSDA2 for a mean value K_y of 0.2.

4.3 Stick-slip Model

As discussed in Section 2.1.4, the stick-slip model is a fully coupled, nonlinear, deformable model developed by Rathje and Bray (2000). This model is coded as a computer program that can be run for multiple earthquake time histories. The inputs are the system properties (T_s, K_y) and the ground motion time history. The program was run for all the selected ground motions and for three different K_y values (0.12, 0.15 & 0.2). A fundamental period of 0.2 seconds was used for the calculations. The output contains two displacements for each time history, considering two polarities of the ground motion, and the average of the two are taken for this study. Figure 4-9(a) and (b) shows the displacements obtained, plotted against PGA of the ground motion and arias intensity. It can be seen that the

variation of displacements for a given I_a is much lower compared that of PGA. This shows that I_a is a better *IM* to predict seismically-induced displacements (Macedo et al., 2020).

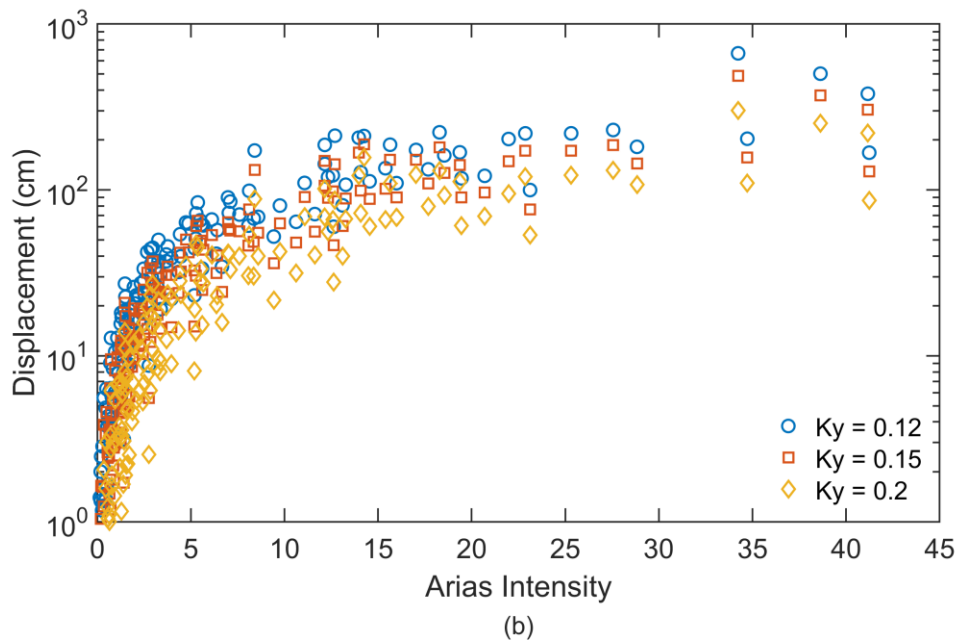
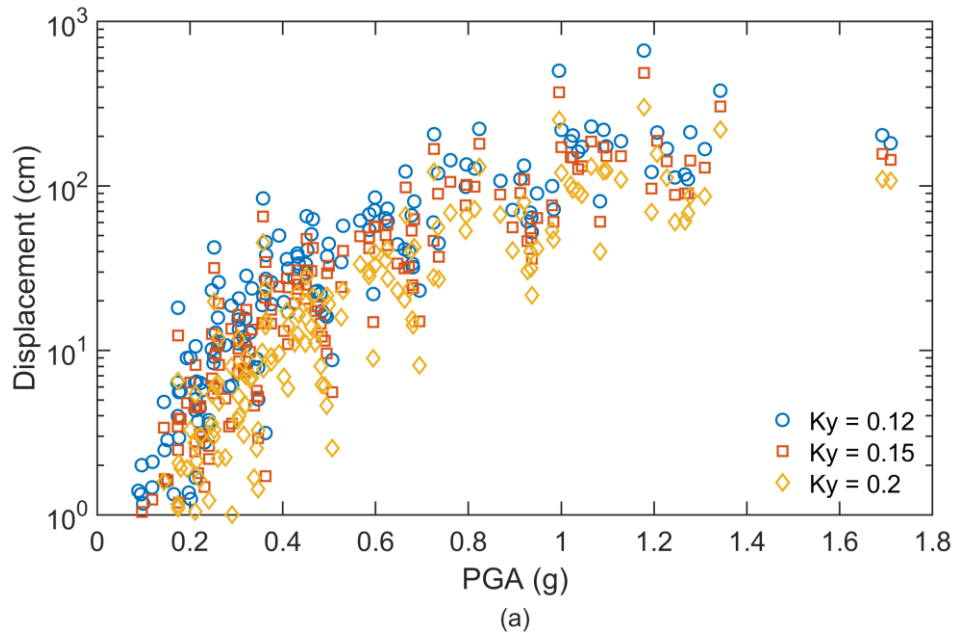


Figure 4-9 (a) Input PGA and displacements, (b) Arias Intensity and displacements obtained from stick-slip model for different K_y values.

4.4 Transfer Function Model

The transfer function model, discussed in Section 2.1.5, estimates a transfer function for the potential sliding mass based on the system properties such as K_y , H , shear wave velocity of the fill (V_s), from which the displacements can be calculated. Similar to the previously discussed stick-slip model, the output consists of two displacements, considering two polarities of the ground motion. The average estimated displacement is considered in this study. The model is run for all the ground motions considering different K_y values (0.12, 0.15, 0.2). The H and V_s are chosen such that the fundamental period (T_s) of the dam is 0.2 seconds when calculated using,

$$T_s = 3H/V_s \quad (7)$$

Figure 4-10(a) and (b) shows the displacements plotted against the *PGA* of the input ground motion and arias intensity. It is important to note that this model is developed based on results from equivalent-linear simulations (Hale, 2019) and calculates displacements using a decoupled approach. Figure 4-11 presents a comparison of displacements obtained from stick-slip method and transfer function model for K_y value of 0.15. It can be observed that the stick-slip model tends to calculate higher displacements for a given *PGA* compared to transfer function model.

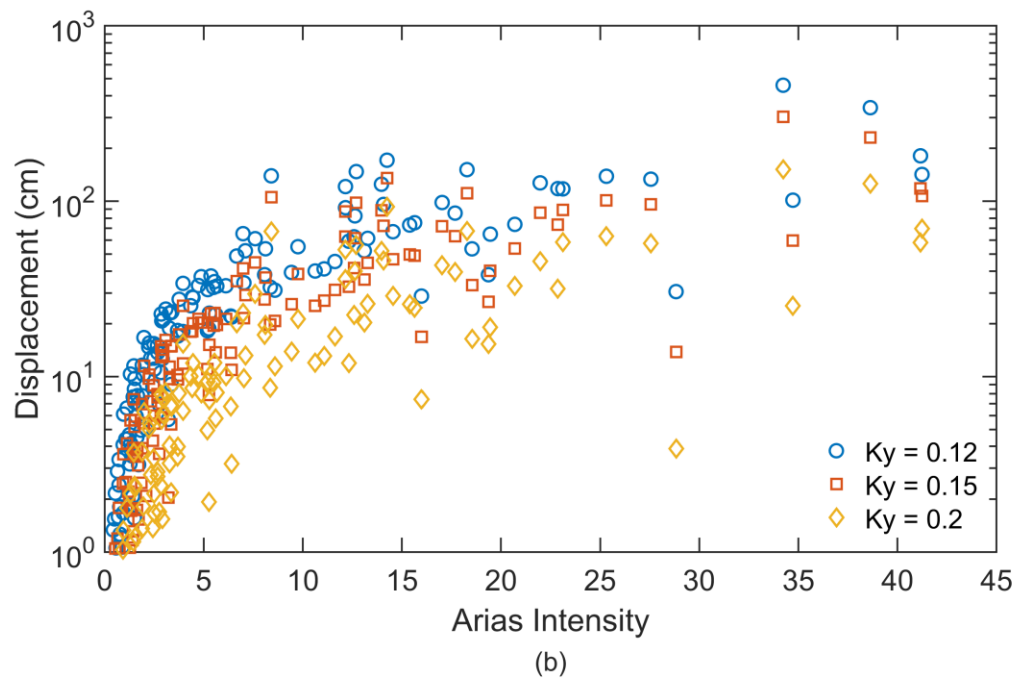
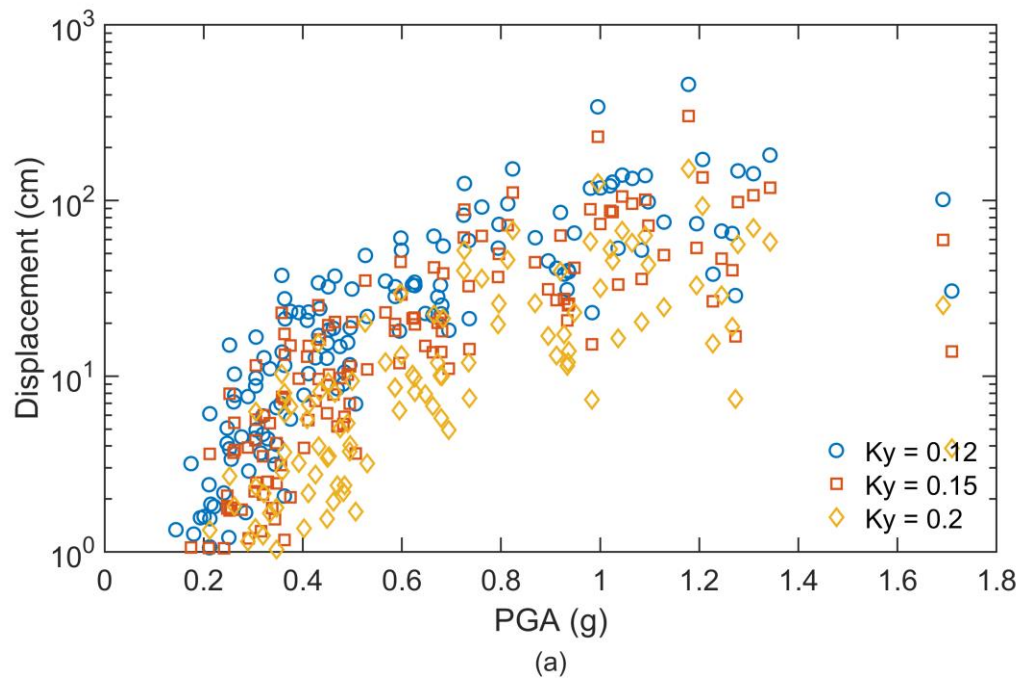


Figure 4-10 (a) Input PGA and displacements, (b) Arias Intensity and displacements obtained from Transfer function model for different K_y values.

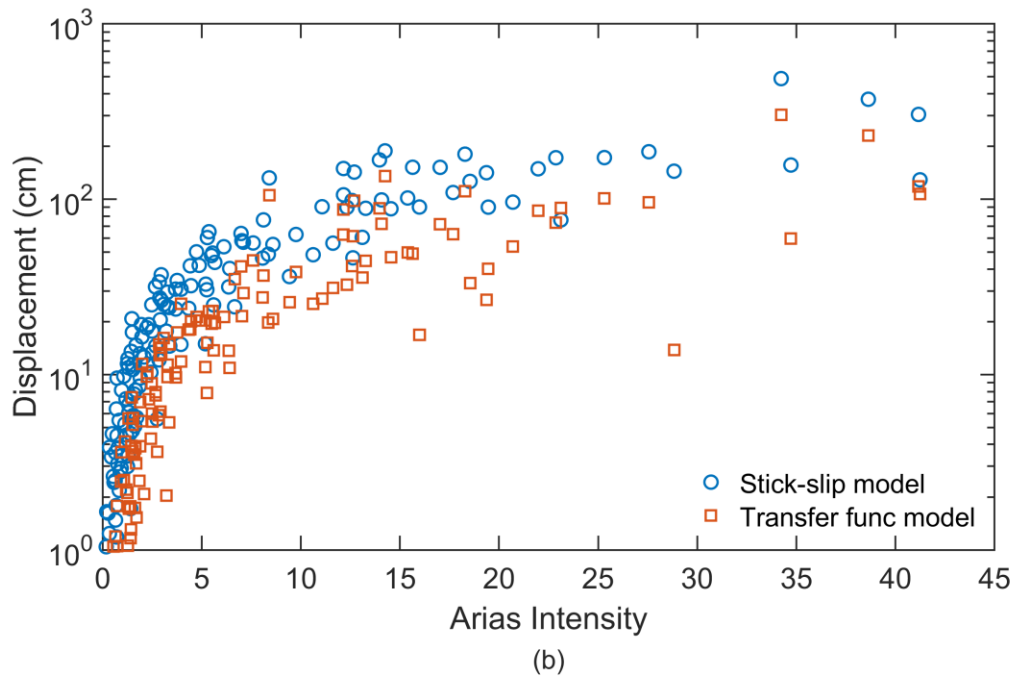
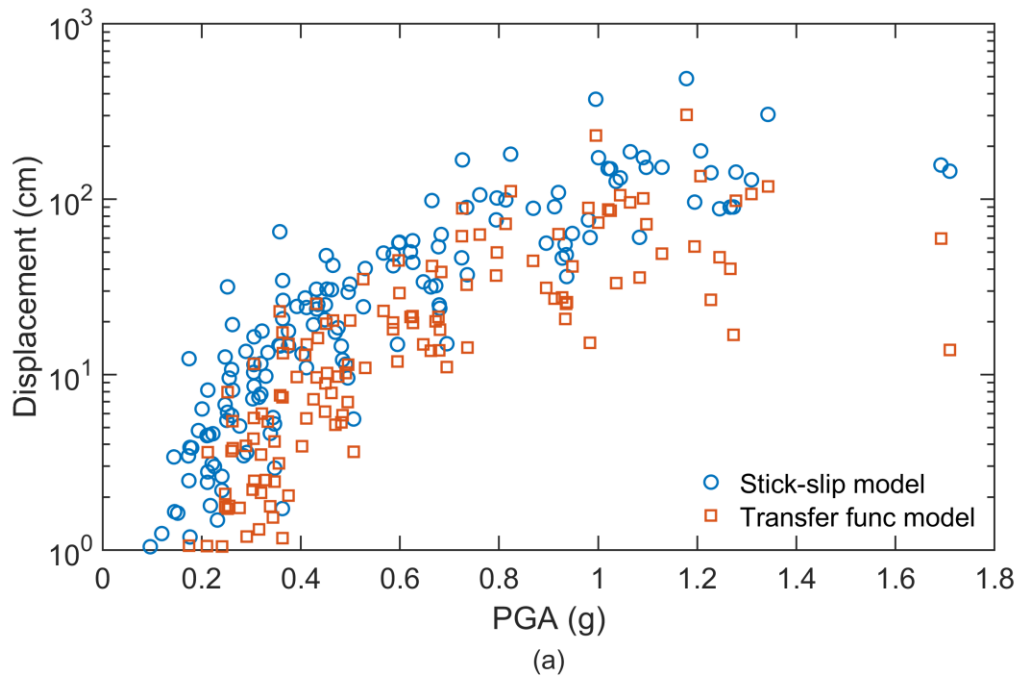


Figure 4-11 Comparison of displacements obtained from transfer function model and stick-slip model for a K_y value of 0.15.

4.5 Displacement Hazard Curves

The deformations associated with each selected time histories and the corresponding rate of occurrence are used to compute seismically-induced displacement hazard curves using the equation,

$$v(def > D) = \sum_{i=1}^{N_{TH}} rate(TH_i) * P(def > D|TH_i, \alpha_i) \quad (8)$$

In this equation, $v(def > D)$ is the rate of exceedance of a given displacement, $rate(TH_i)$ is the rate assigned to the i^{th} time history, $P(def > D|TH_i, \alpha_i)$ is the conditional probability that the deformation resulting from the scaled time history is greater than the selected deformation threshold (D). It is either 1 or 0.

Figures 4-12(a), 4-13(a), and 4-14(a) shows the displacement hazard curves obtained from the analytical procedures discussed above for different K_y values. As discussed earlier, it is evident that the displacement given a hazard level decreases as K_y increases. The displacement hazard curve from stick-slip model is above the transfer function model, which may be because of the difference in their formulation. This transfer function model relies on estimation of a transfer function and decoupled analysis, whereas the stick-slip model is based on a generalized SDOF system and coupled analysis. Figures 4-12(b), 4-13(b), and 4-14(b) show the histograms of displacements from stick-slip model and TFM. The values in the y-axis of this plot shows the frequency of displacements in various bins. A bin size of 5 cm was selected. It can be observed that the transfer function model produces more lower displacements ($D < 5\text{cm}$) and stick-slip model produces more high displacement values. This explains why the *DHC* from stick-slip model is above the *TFM*

for lower displacement thresholds and becomes more comparable as displacement increases. Figures 4-12(c), 4-13(c), and 4-14(c) present summed rate of occurrences for different displacement bins. The values in the y-axis of this plot are calculated by summing up the rate of occurrences of ground-motions that produced displacement values in that respective bin. It is interesting to see that the ground-motions causing lower displacements have high rate of occurrences (i.e., they are more frequent) and ground-motions causing higher displacements are associated with low rate of occurrences (i.e., they are less frequent).

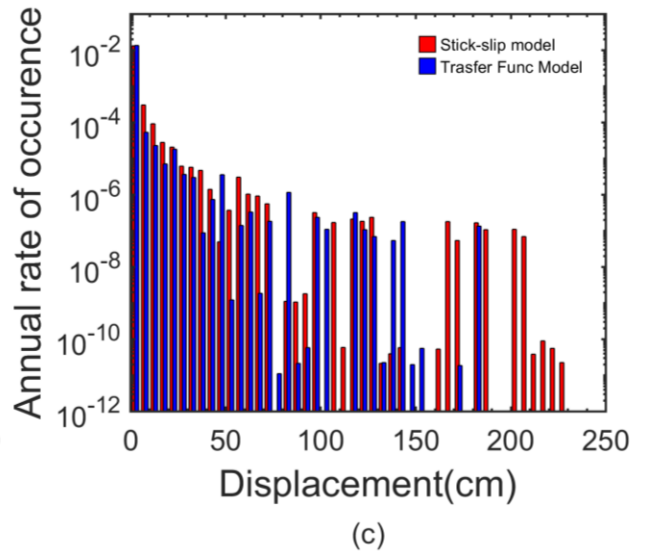
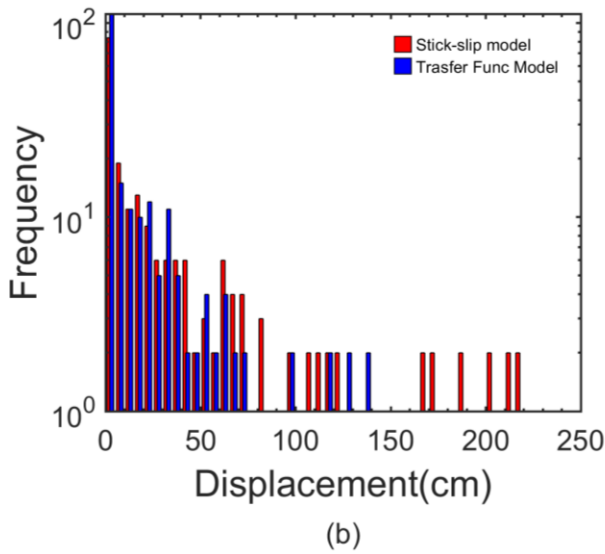
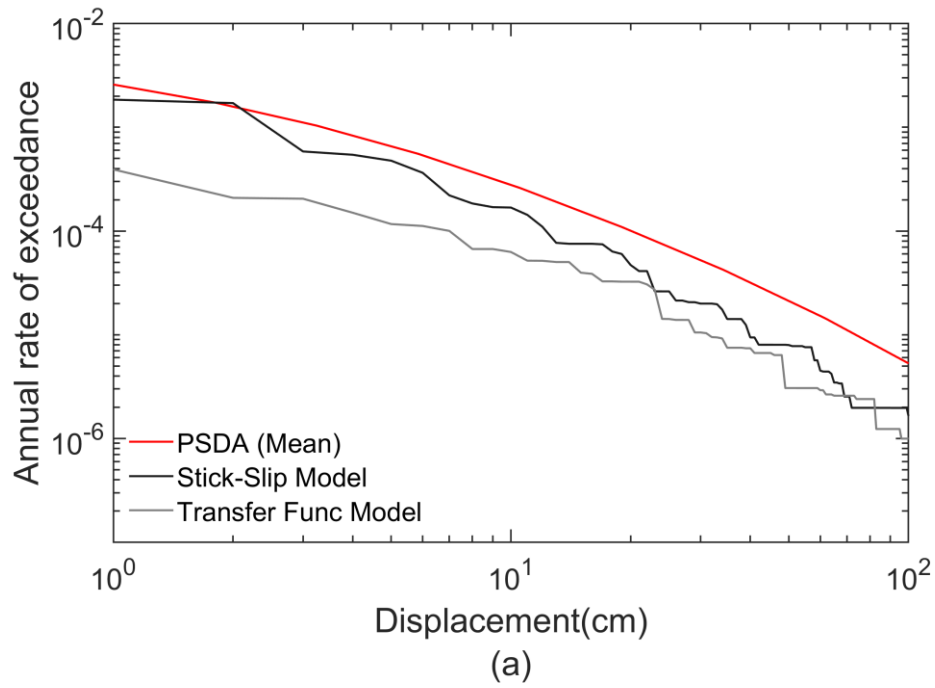


Figure 4-12 Comparison of (a) displacement hazard curves (b) histograms of displacements (c) summed rate occurrences for displacement bins obtained from analytical procedures for a K_y value of 0.12.

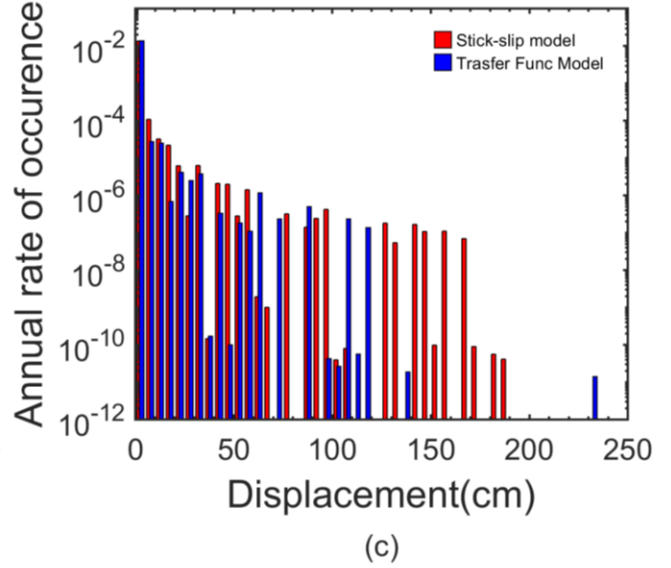
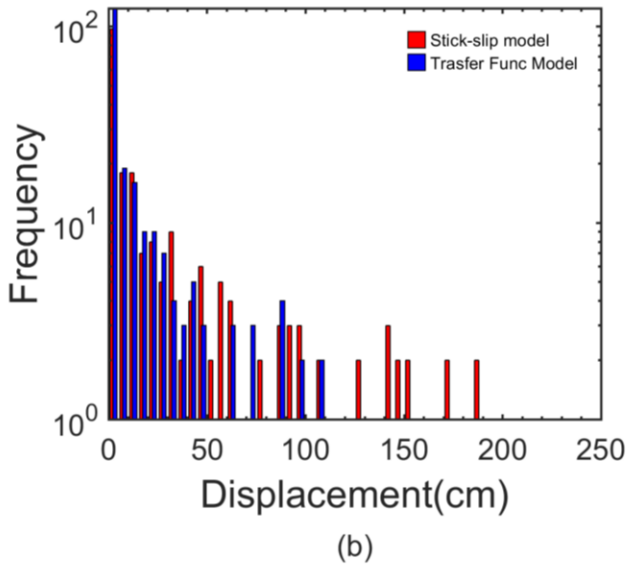
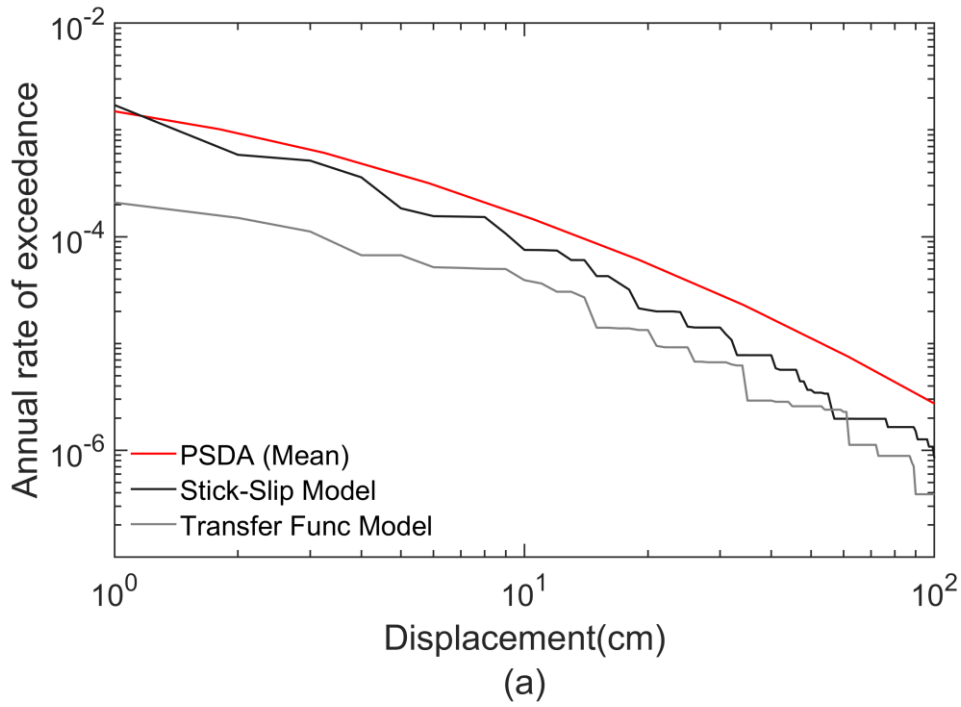


Figure 4-13 Comparison of (a) displacement hazard curves (b) histograms of displacements (c) summed rate of occurrences for displacement bins obtained from analytical procedures for a K_y value of 0.15.

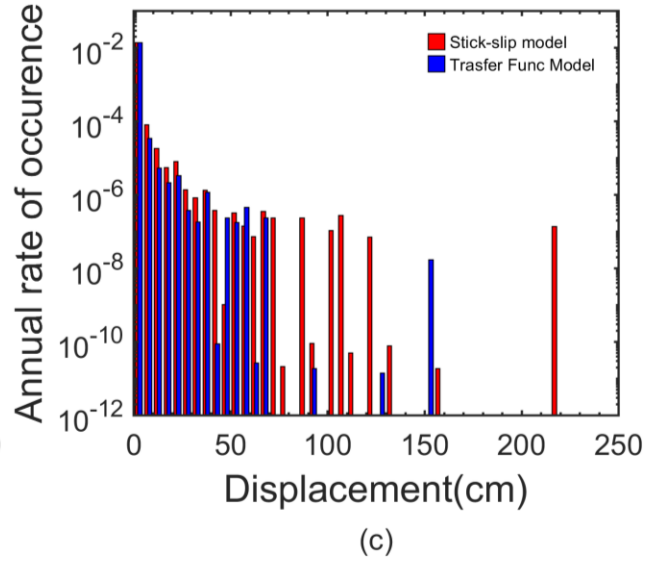
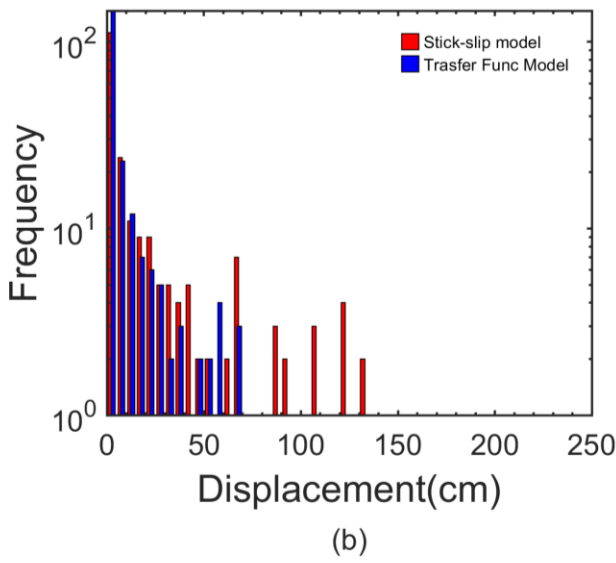
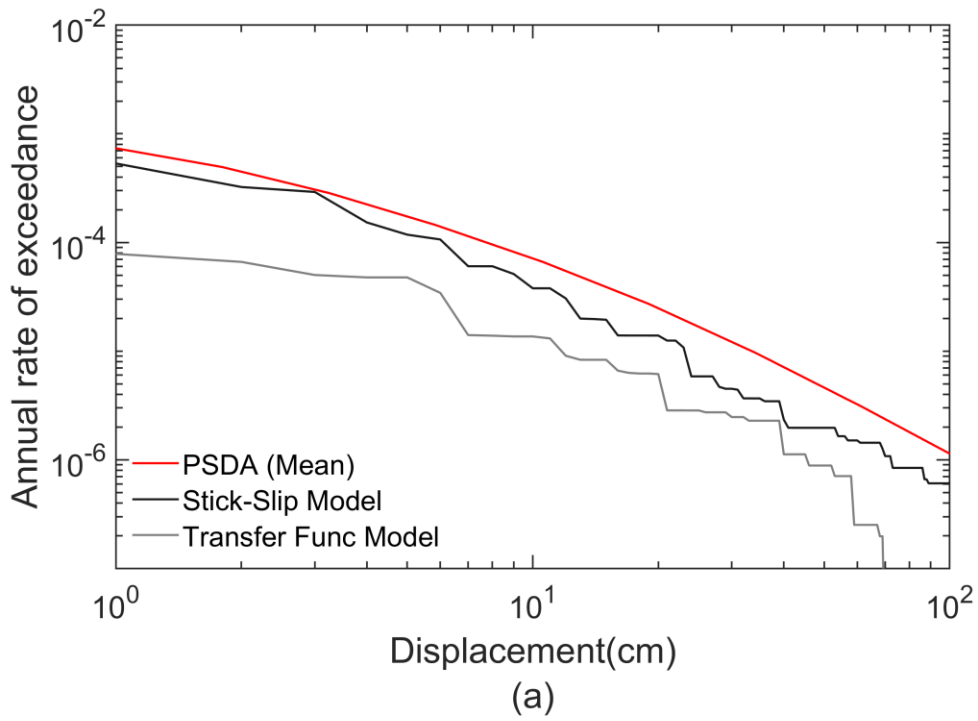


Figure 4-14 Comparison of (a) displacement hazard curves (b) histograms of displacements (c) summed rate of occurrences for displacement bins obtained from analytical procedures for a K_y value of 0.2.

CHAPTER 5. DYNAMIC ANALYSIS

5.1 Dam geometry

The nonlinear dynamic analyses (NDA) were performed using the program Fast Lagrangian Analysis of Continua (FLAC; Itasca, 2016). This program is well suited for performing dynamic analysis with nonlinear material response using user defined constitutive models. The dam was modeled in a plane strain condition. The size of the elements in FLAC were selected such that they ensure accurate wave transmission based on Kuhlemeyer and Lysmer (1973). The size of the elements ranged from 1.2 to 1.4 meters in the vertical and horizontal directions, respectively. Figure 5-1 shows the prepared mesh for the model and the five zones, which are divided depending on the range of stresses, as elaborated below.

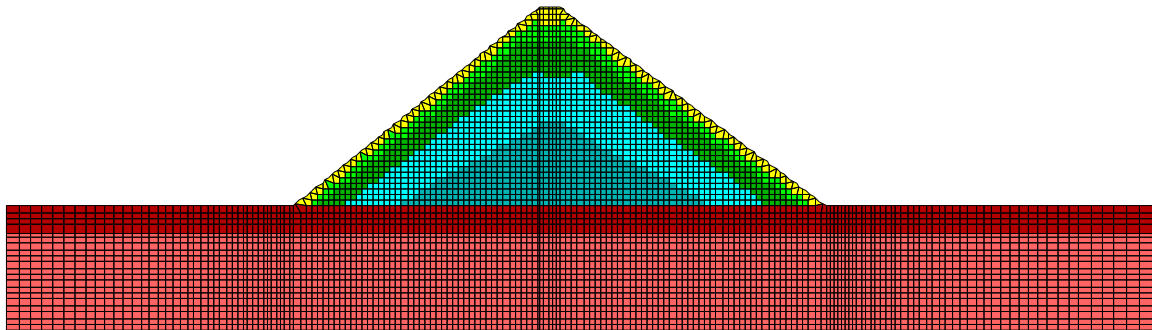


Figure 5-1 Numerical Mesh and the dam model.

5.2 Calibration of Constitutive Models

The nonlinear behavior of the dam fill was modelled in FLAC using three different constitutive models namely UBCHyst (Byrne and Naesgaard, 2015), PM4Sand (Boulanger

and Ziotopolou, 2017), and Wang 2D (Wang 1990; Wang et al., 1990; Wang and Ma, 2018). The elastic-perfectly plastic Mohr-coulomb model was used for the materials in the foundation. The constitutive models were calibrated against the modulus reduction and damping curves obtained from the literature (Figure 2-4). Based on the literature review performed for this study, it was found convenient to calibrate the models to fall between lower bound of Seed et al. (1986) and upper bound of Rollins et al. (1998) in order to reasonably reproduce the dynamic response of an “average” rockfill material. The dam embankment was divided into five different layers based on the vertical stresses as presented in Table 3, this was done to account for changes in the parameters of constitutive models in terms of stresses. The shear modulus of the foundation materials was kept constant, the lower shear wave velocity profile from Hale (2019) was adopted for the dam embankment, and finally the maximum shear modulus was calculated from the V_s profile using,

$$G_{max} = \rho V_s^2 \quad (9)$$

where, G_{max} is the maximum shear modulus, ρ is the density of the material, V_s is the shear wave velocity.

Table 3 Different layers based on confinement.

Layers	Confinement (kPa)
1	<75
2	75 < 150
3	150 < 300
4	300 < 550
5	550 < 1000

In the following, a brief summary of the constitutive models used in this study are presented and the calibration process is described. The calibration was performed independently for each one of the layers presented in Figure 5-1.

5.2.1 UBCHyst

The UBCHyst (Byrne and Naesgaard, 2015) is a two-dimensional, total stress hysteretic soil model. The UBCHyst model is framed to capture the dynamic behavior of soils such as low permeable clays, high permeable granular soils, in which there will be no generation of excess pore pressure. The model uses a Mohr-coulomb failure criterion, extended with a tangent shear modulus, which is a function of stress ratio and the change in stress ratio to reach failure. This function is shown in Equation 10 and illustrated in Figure 5-2.

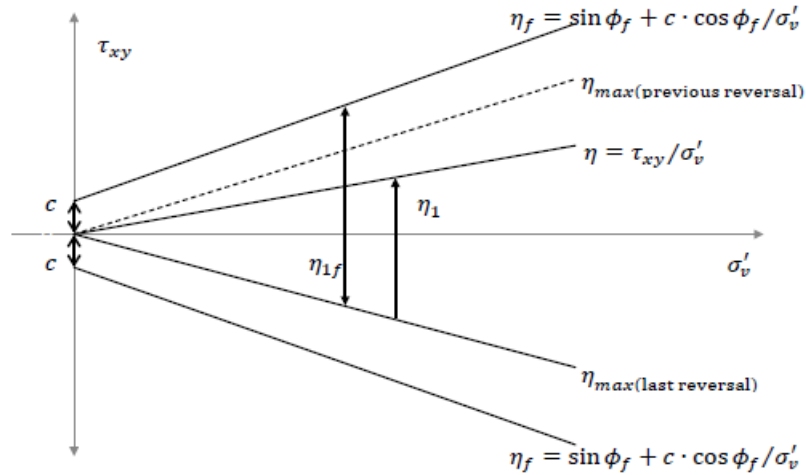


Figure 5-2 UBCHYST model key variables (Byrne and Naesgaard, 2015).

$$G_t = G_{max} \left(1 - \left(\frac{\eta_1}{\eta_{1f}} \right)^{n_1} R_f \right)^n \times mod1 \times mod2 \times mod3 \quad (10)$$

where,

ϕ_f = peak friction angle

G_r = reference shear modulus

η = current stress ratio = τ_{xy}/σ_v'

η_1 = change in stress ratio since last reversal ($\eta - \eta_{max}$)

η_{max} = maximum stress ratio at last reversal

η_{1f} = change in stress ratio to reach failure envelope in direction of loading ($\eta_f - \eta_{max}$)

$\eta_f = (\sin(\phi_f) + Cohesion \times \cos(\phi_f))/\sigma_v'$

τ_{xy} = developed shear stress in horizontal plane

σ_v' = vertical effective stress

$mod1$ = a reduction factor for first-time or virgin loading

$mod2$ = optional function to account for permanent modulus reduction with large strain

$mod3$ = optional function to account for cyclic degradation of modulus with strain or number of cycles

n , n_1 and R_f are calibration parameters

The effect of each parameter associated with the shear modulus reduction and damping was studied by setting all parameters to recommended values and varying each parameter one at a time. Of the 11 input parameters the following six were modified for this study: maximum shear modulus (G_{max}), bulk modulus, friction angle, hysteric parameters (n , R_f , R_m). The first three parameters were calculated based on average material properties of each layer. The effective friction angle is considered as a function of confinement and calculated based on Barton and Kjaernsli (1981),

$$\phi' = R \log(S/\sigma'_n) + \phi_b \quad (11)$$

where, ϕ_b is the base friction angle, R is the equivalent roughness of the actual rock particles, S is the compressive strength of the parent rock, and σ'_n is the effective normal stress. For this study, a base friction angle of 25 degrees, an equivalent roughness of 7.5 and a compressive strength of 16 MPa was used. The last three parameters (n, R_f, R_m) were used to calibrate the modulus reduction and damping relation of the model. Figure 5-3 presents the calibrated UBCHyst modulus reduction and damping curves for each layer.

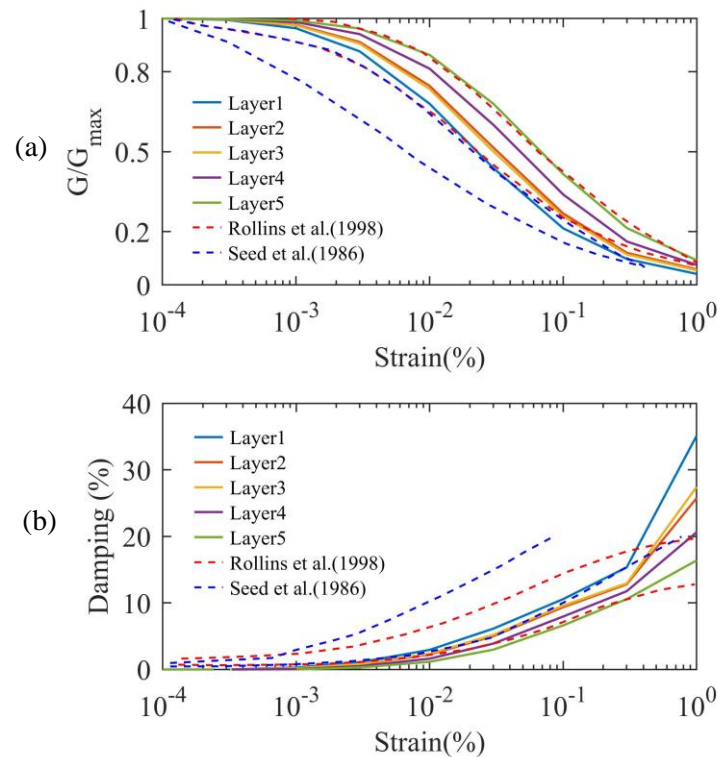


Figure 5-3 Calibrated modulus reduction and damping curves for UBCHyst model.

5.2.2 PM4 Sand

The PM4Sand (Version 3.1) (Boulanger and Ziotopolou, 2017), as described in the user manual (Boulanger and Ziotopolou, 2017), follows the basic framework of the stress-ratio

controlled, critical state compatible, bounding surface plasticity model for sand initially presented by Dafalias and Manzari (2004). PM4Sand is formulated by modifying this model. This model incorporated a critical state line that is consistent with Bolton's (1986) dilatancy relationship. Figure 5-4 shows the bonding, dilatancy and critical surfaces as lines in q-p space adopted from Dafalias and Manzari (2004).

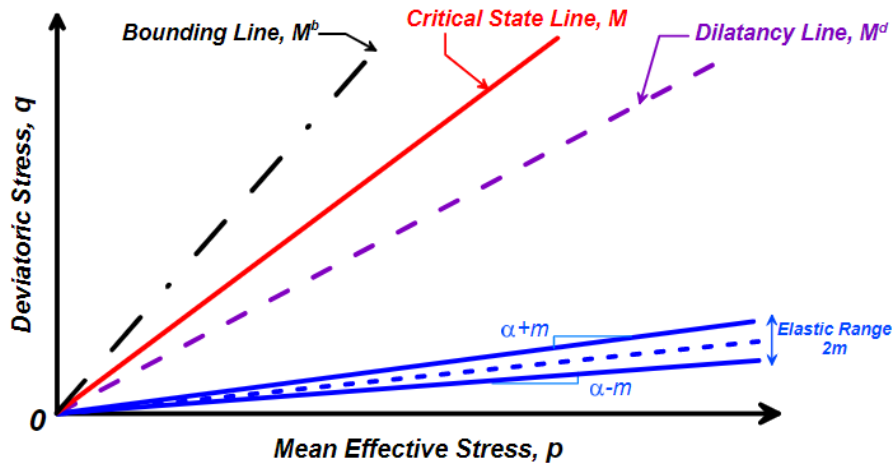


Figure 5-4 Schematic of yield, critical, dilatancy and bonding lines in q-p space. (from Boulanger and Ziotopolou, 2017).

PM4Sand consists of five primary parameters and eighteen secondary parameters. The primary parameters include density (ρ), porosity (n), relative density (D_r), shear modulus coefficient (G_o), contraction rate parameter (h_{po}), and atmospheric pressure (P_a). The secondary parameters are described in Boulanger and Ziotopolou (2017). A constant value of G_o is used for all layers and is calculated using,

$$G = G_o p_a (p/p_a)^{1/2} \quad (12)$$

where, G is the elastic shear modulus, which is calculated using Equation 9, p is the mean pressure.

The parameters D_r and h_{p0} were considered as free parameters and were used to adjust the modulus reduction response of the model. All the secondary parameters were set as default except for the effective friction angle, which is calculated using Equation 11. In addition, the generation of excess pore pressures was prevented so the constitutive model can represent the response of a fully drained granular material such as a rockfill. Figure 5-5 presents the modulus reduction and damping curves calibrated for PM4Sand model.

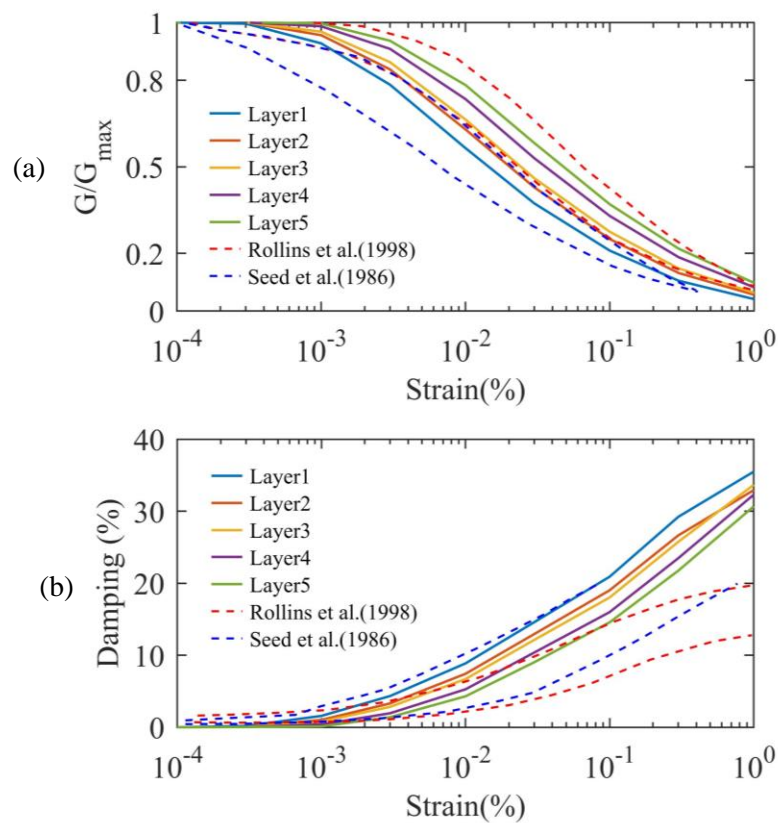


Figure 5-5 Calibrated modulus reduction and damping curves for PM4Sand model.

5.2.3 Wang 2D model

The Wang2D (Wang 1990; Wang et al., 1990; Wang and Ma, 2018) is a two-dimensional version of the original three-dimensional model, which is a bounding surface plasticity

model developed for modeling sand behavior under different loading conditions ranging from simple monotonic to complex cyclic loading. One distinctive feature of this model is the dependence of the loading and plastic strain rate directions on the stress rate directions (Chowdhury, 2019). The Wang 2D and PM4Sand model share a number of common attributes.

Only four out of the eleven input parameters are needed to calibrate the modulus reduction response of the model since the generation of excess pore pressures is prevented (Wang and Ma, 2018). These four parameters are shear modulus coefficient (G_o), effective friction angle (ϕ'), Poisson's ratio (ν), and h_r . The remaining parameters retained the default recommended values. The value of G_o is maintained constant for all the layers and is calculated using Equation 12. The ϕ' is estimated using Equation 11 and a constant value ν is used throughout the fill. The parameter h_r characterizes the nonlinear relationship between shear modulus and shear strain amplitude and is used for the calibration of the shear modulus reduction and damping curves. Figure 5-6 presents the modulus reduction and damping curves calibrated for the Wang2D model.

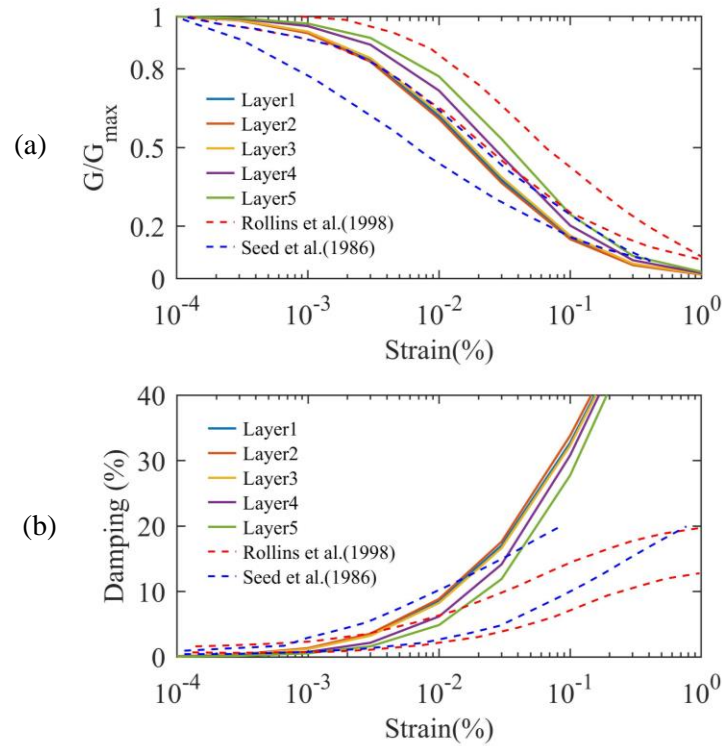


Figure 5-6 Calibrated modulus reduction and damping curves for Wang2D model.

5.3 Static Analysis

The pre-earthquake static analysis is important as it serves as the initial condition for the dynamic analysis. The steps in static analysis include 1) mesh and soil zones generation 2) material property assignment with elastic-perfectly plastic Mohr-Coulomb model 3) construction of the dam embankment to develop initial effective stress 4) steady-state seepage analysis 5) constitutive model assignment. Although the construction sequence of the dam was not modeled, the embankment was constructed by turning on the gravity in ten steps to create more realistic stress states.

During the static analysis, the base of the model was fixed in both the horizontal and vertical directions. The left and right vertical boundaries were fixed to prevent horizontal

displacements. A hydrostatic pressure is applied to the upstream boundary and the pore pressures on the upstream boundary are defined by the reservoir head (43m/141 ft). A steady state seepage analysis is performed to develop the initial phreatic surface inside the dam. The initial vertical, horizontal, and pore pressure contours are shown in Figures 5-7, 5-8, and 5-9.

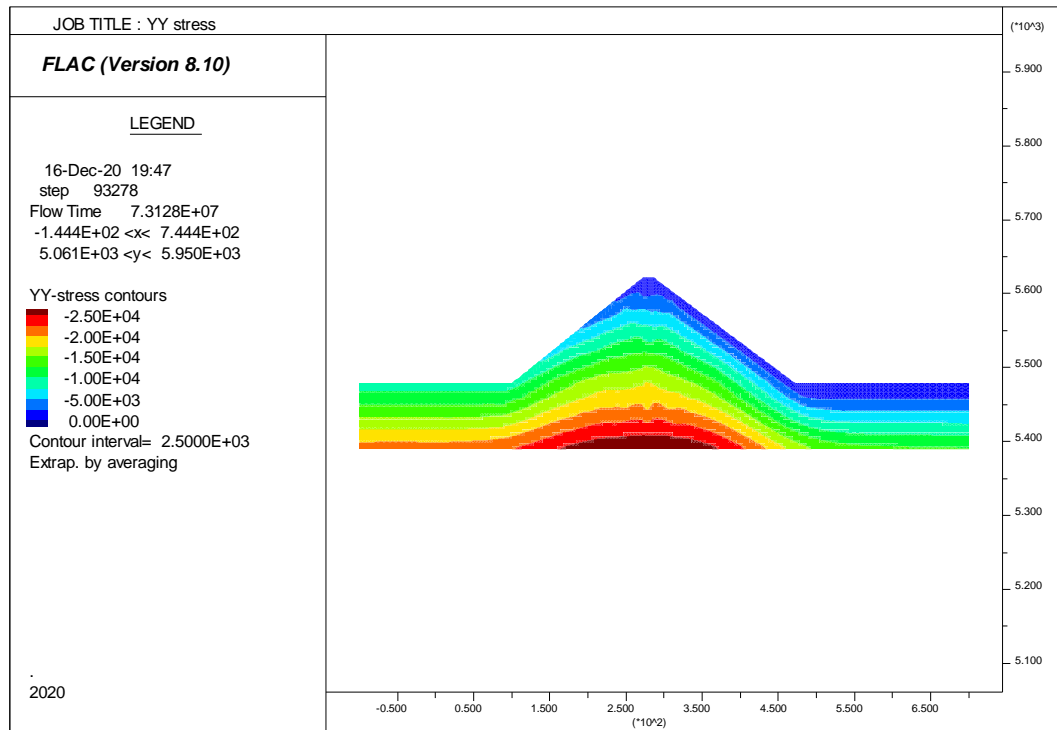


Figure 5-7 Initial static vertical stress contours.

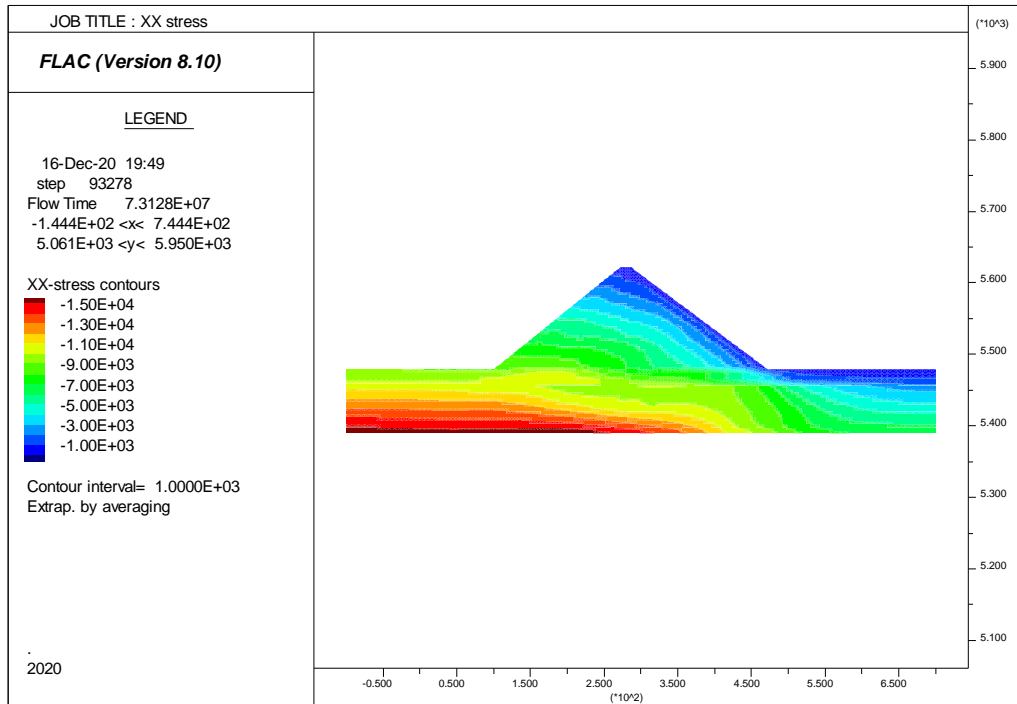


Figure 5-8 Initial static horizontal stress contours.

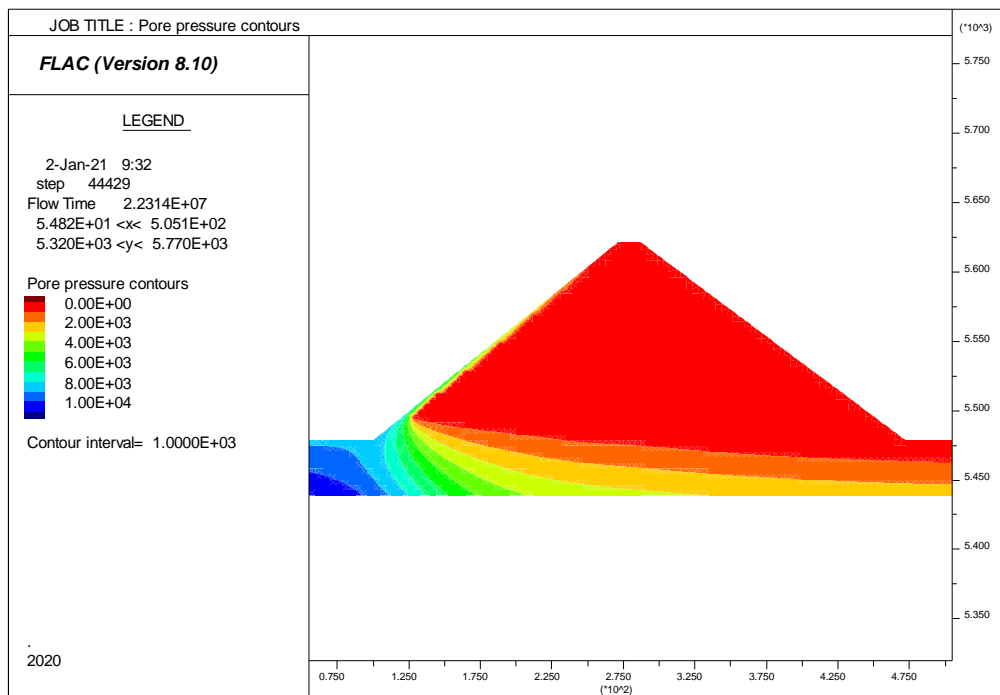


Figure 5-9 Initial static pore pressure contours.

5.4 Dynamic Analysis

The stress conditions from static analysis serve as the initial conditions for the dynamic analysis. A free-field condition was applied on the vertical edges in both upstream and downstream sides to avoid spurious reflections. The vertical boundaries are located at a significant distance from the dam, to minimize the boundary effect in the analyses. A compliant base boundary condition is applied to the bottom of the model by applying a quite boundary condition in both x and y directions. The ground-motions are applied to the base of model by converting the velocity time history to a shear stress (σ_s) time history using,

$$\sigma_s = \rho V_s v_s \quad (13)$$

where, ρ and V_s are the density and the shear wave velocity of the base material, and v_s is the shear component of the particle velocity at the boundary. A small Rayleigh damping is also applied to the model ($\xi_{min} = 0.2\%$ at $f_{min} = 2.8$ Hz). The analyses were run with all selected ground-motion time histories using three different constitutive models, a total of 660 dynamic analyses were performed.

CHAPTER 6. RESULTS FROM DYNAMIC ANALYSIS

6.1 Comparison of Constitutive Models

The results from the dynamic analyses along with key observations are discussed in this section.

6.1.1 PGA vs Displacement

Figure 6-1 and Figure 6-2 presents the horizontal displacement obtained from a point in the downstream slope and the vertical crest displacement versus the input PGA for all three constitutive models. Wang2D model shows the lowest displacements in both the cases. It can be seen that, for low intensity ground-motions ($PGA < 0.2g$), PM4Sand shows the highest displacement whereas for moderate to high intensity ground-motions ($PGA > 0.2g$), UBCHyst gives the highest displacements in both directions.

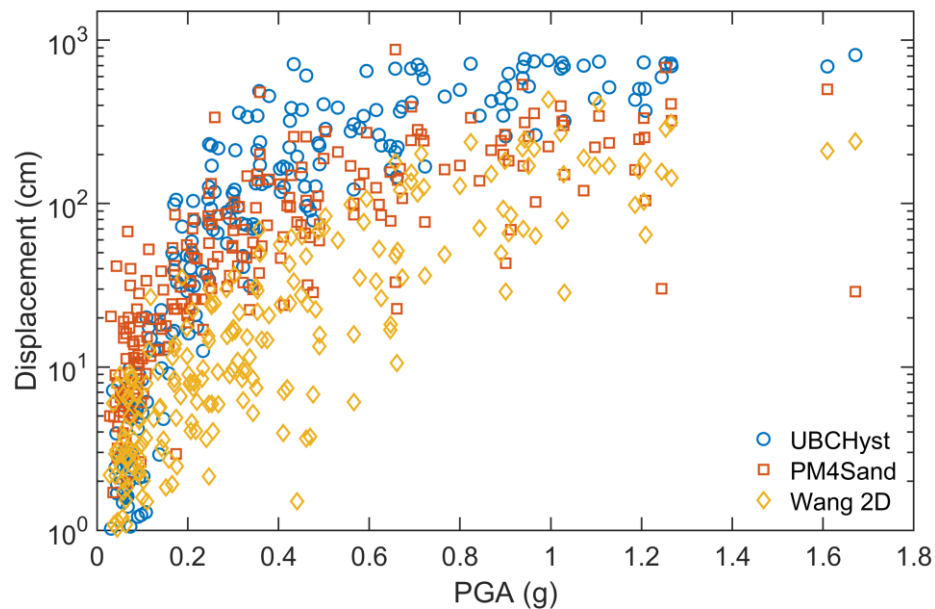


Figure 6-1 Horizontal displacement at a point in the downstream slope and input PGA.

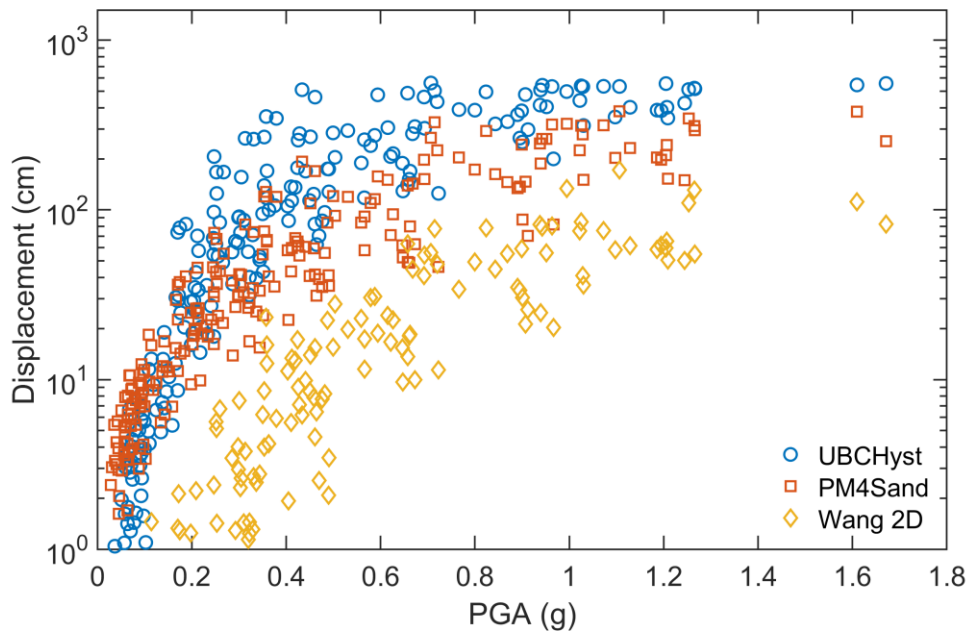


Figure 6-2 Vertical displacement in the crest area and input PGA.

6.2 Displacement Hazard Curves

The displacement hazard curves are calculated using Equation 8. Figure 6-3 shows the horizontal displacement hazard curves for a point in the downstream slope and 6-4 presents the vertical displacement hazard curves constructed using permanent displacements in the crest area for the three models. The horizontal displacement hazard curve from PM4Sand model gives the highest displacements for a given hazard level (or return period). In terms of vertical displacements, given a hazard level, the displacements estimated from the PM4Sand model are the highest for displacement thresholds lower than 10 cm. For displacement thresholds higher than 10cm, the displacements estimated from the UBCHyst model are the highest. Though UBCHyst provides overall higher displacements for large intensity ground motions (Figure 6-1 and 6-2), the displacement hazard curve calculated from PM4Sand is above the displacement hazard curve from UBCHyst. This is because,

the displacements from PM4Sand model are higher for low to moderate intensity ground-motions (Figure 6-1 and 6-2), which have a higher rate of occurrence compared to high intensity ground-motions. From a risk perspective, the ground-motions with moderate rate of occurrence which cause moderate displacement demands are of more interest compared to ground-motions causing higher displacements.

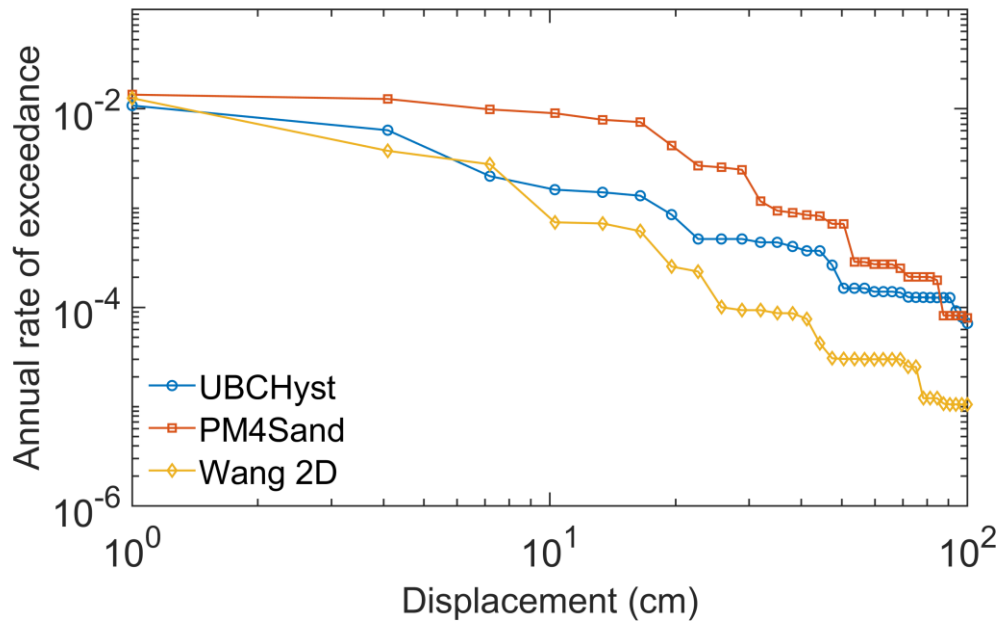


Figure 6-3 Horizontal displacement hazard curves at a point in the downstream slope from dynamic analysis.

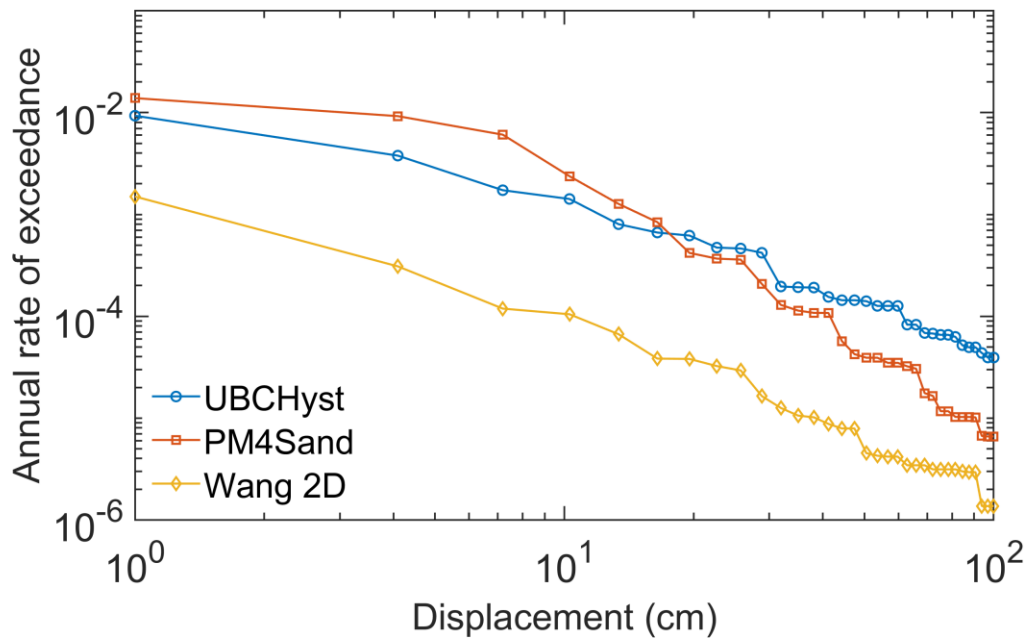


Figure 6-4 Vertical displacement hazard curves in the crest area from dynamic analysis.

In the downstream slope, displacement histories were recorded in a sliding surface representative of the sliding surface for a K_y of 0.12 (Figure 4-2), and the results were used to estimate representative displacement hazard curves by averaging the recorded values. Figure 6-5 shows the median and maximum total displacement hazard curves computed using all three models. The median displacement hazard curve for Wang 2D model is not presented as the displacements within the failure surface were not recorded due to computational constraints in the simulations.

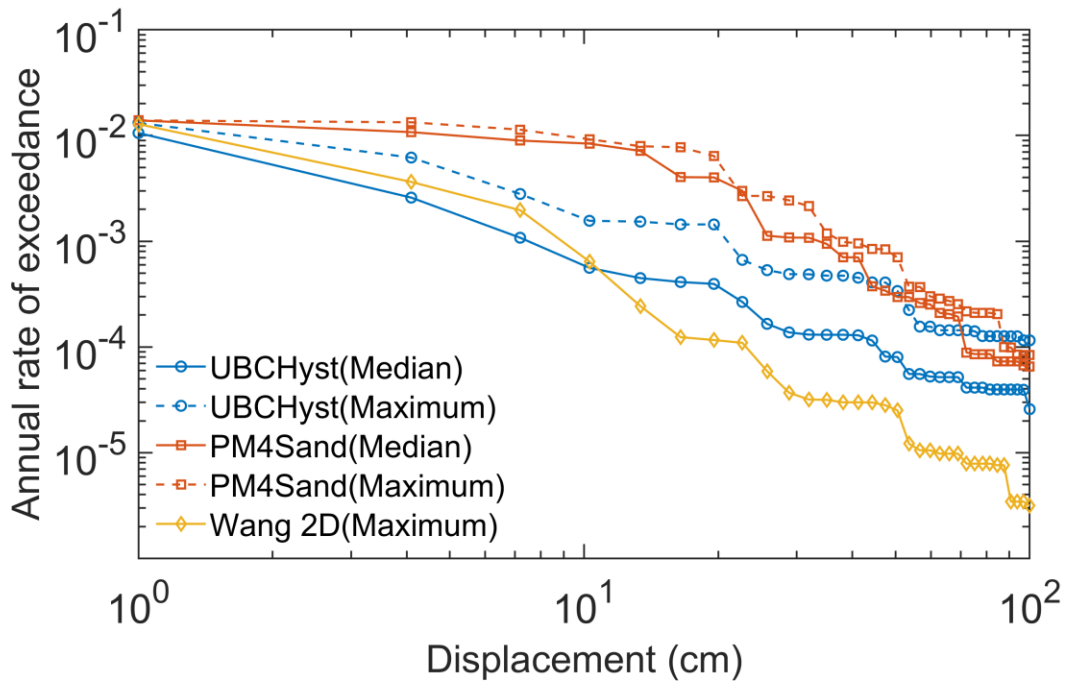


Figure 6-5 Median and maximum total displacement hazard curves for all three constitutive models.

To shed lights on the results presented in this section, single element cyclic and monotonic simulations were performed considering the three constitutive models used in the dynamic analyses. For each model, the tests were carried out for five elements, each representing one layer of the fill. The same constitutive model parameters and average material properties of each layer from the dynamic analyses were used in the element level simulations. Figure 6-6 to 6-9 presents the results from the element level analyses for Layers 3 and 5, which is illustrative of the patterns observed for all layers. From Figures 6-8(b) and 6-9(b), we can see that PM4Sand model exhibits larger volumetric strains compared to the other two models which explains the larger displacements obtained from PM4Sand for a given hazard level. Figures 6-8(a) and 6-9(a) also shows the shape of the stress strain loops evidencing that for a comparable level of shear strains the area inside the hysteretic loops is comparable for the UBCHyst and PM4sand models and higher for

the Wang model, which is consistent with the larger damping values in the Wang model and the comparable damping levels from the UBCHyst and PM4Sand models in Figures 6-6(b) and 6-7(b). These observations are consistent with the results in Figures 6-3, 6-4, and 6-5. For example, in the downstream slope area, even though the deviatoric mechanisms are presumed to be more important, there is also an expected contribution from volumetric mechanisms. Hence, because the PM4Sand model has a higher contribution from volumetric mechanisms, it tends to produce higher displacements. This is especially the case for low displacement thresholds in the displacement hazard curves, as the displacement thresholds are increased from moderate to large displacements, the PM4Sand model tends to provide higher damping values compared to the UBCHyst models, which compensates the effects of the contribution from volumetric mechanisms, and the displacements, given a hazard level, from the UBCHyst and PM4Sand models are more comparable. In the case of the Wang model, because the contributions from volumetric mechanisms are lower and the damping is larger, the displacements are lower compared to the other two models.

To understand the behavior of these models at the crest area, where the confinement is much lower, an additional set of element level analyses at a confinement of 10kPa were carried out. Figure 6-10 and 6-11 show the behavior of these models at a confinement of 10 kPa. From Figure 6-11(b), it can be seen that, for a lower confinement the PM4Sand model shows a contractive behavior for lower strains and a dilative behavior for higher strains. This explains the trend seen in Figure 6-2, for low displacement thresholds where the strain imposed is lower, the vertical displacement hazard curve from PM4Sand is higher because of the contractive behavior and for high displacement thresholds where the strain

imposed is higher, the displacements from PM4Sand for a given a hazard level are lower than that from UBCHyst because of the dilative behavior.

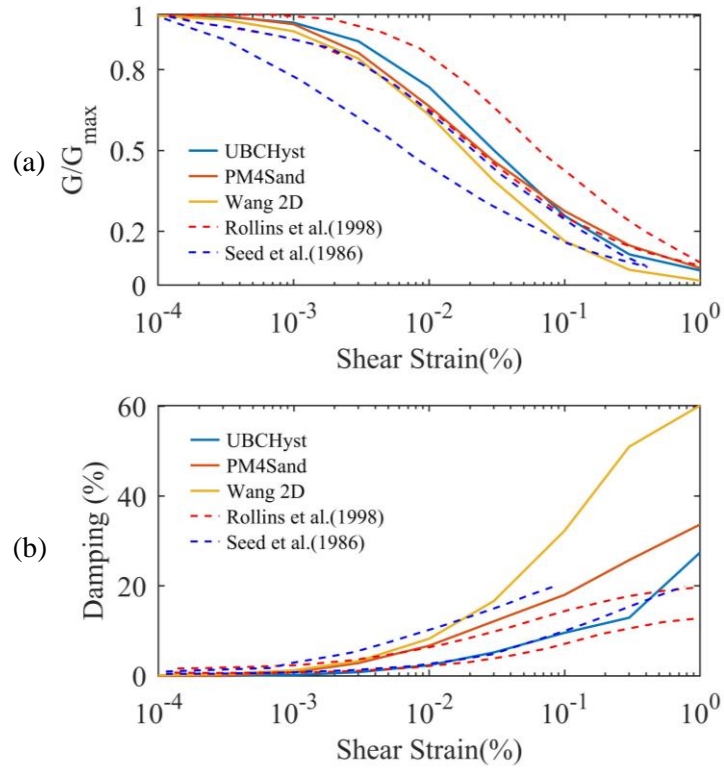


Figure 6-6 Modulus reduction and damping curves for Layer 3.

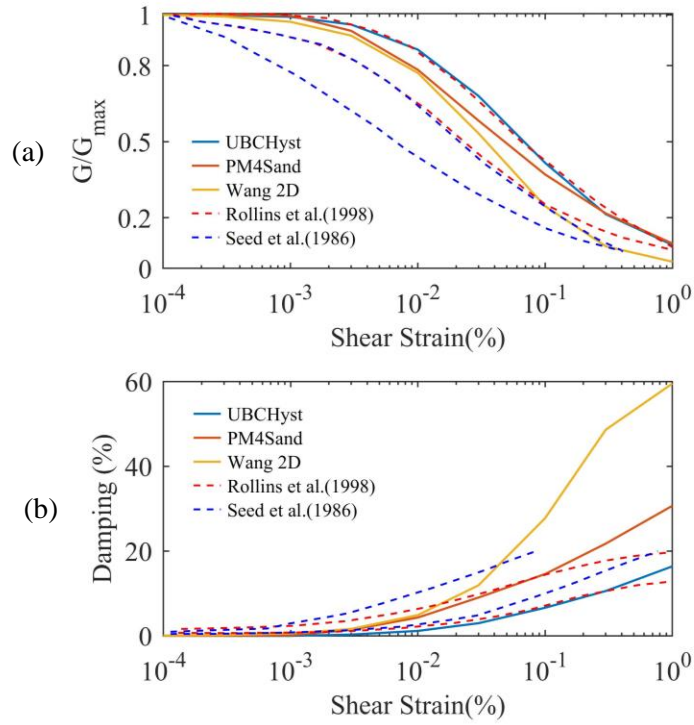


Figure 6-7 Modulus reduction and damping curves for Layer 5.

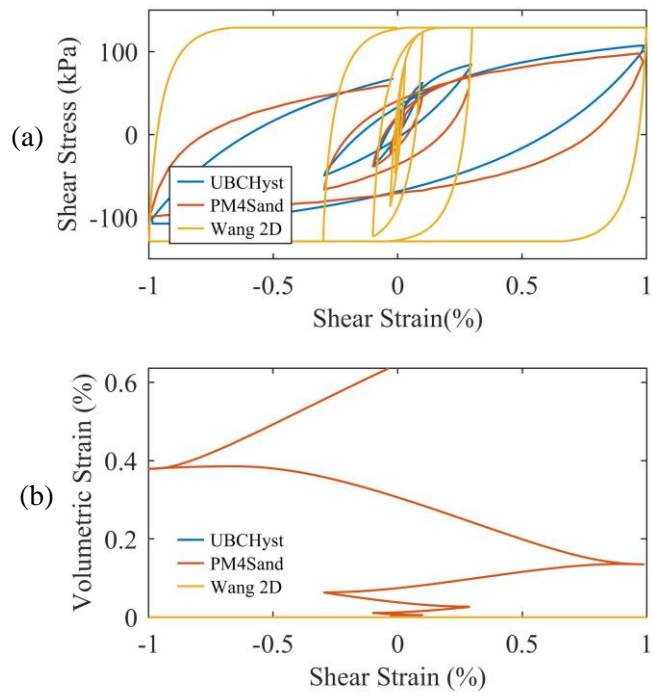


Figure 6-8 Results from cyclic direct simple shear test for Layer 3.

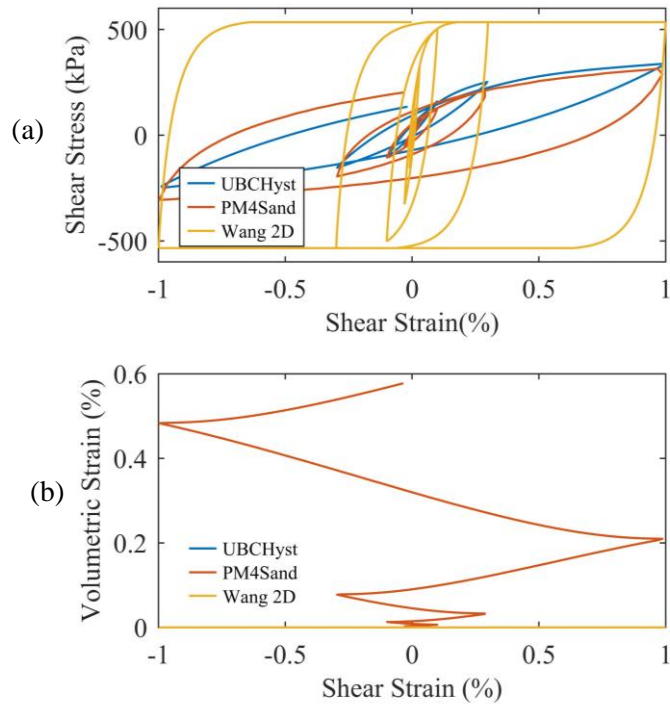


Figure 6-9 Results from cyclic direct simple shear test for Layer 5.

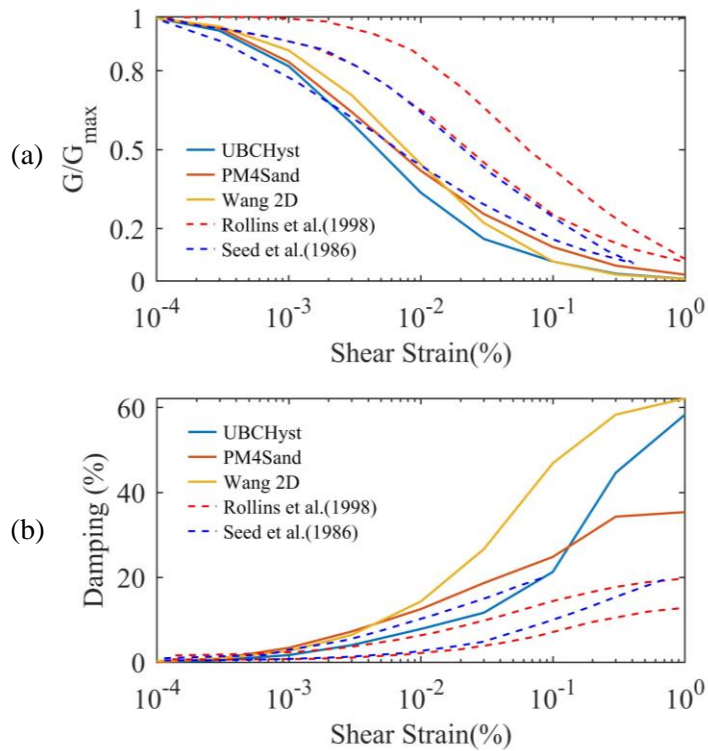


Figure 6-10 Modulus reduction and damping curves for a confinement of 10 kPa.

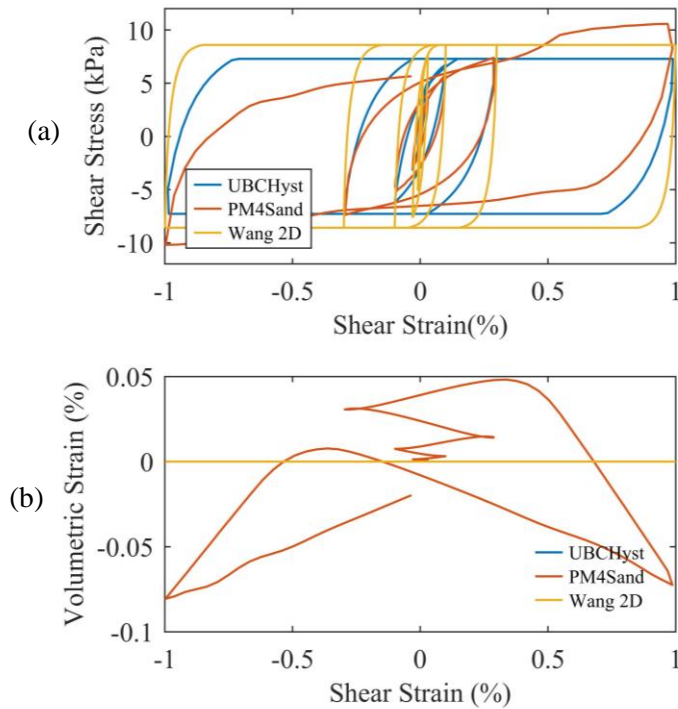


Figure 6-11 Results from cyclic direct simple shear test for a confinement of 10 kPa.

6.3 Comparison with analytical procedures

Figure 6-12 shows the comparison of displacement hazard curves obtained from analytical methods and nonlinear dynamic analyses. The results from analytical methods for a K_y value of 0.12 are used for the comparison. Given a hazard level, the displacements estimated from analytical methods are lower compared to those from numerical analyses. The comparison of displacements for two representative returns periods are presented in Table 4. For example, for a return period (T_R) of 475 years, the range of displacements from analytical procedures are 0 to 1.5 cm (PSDA) while the displacements from NDA ranges from 5 cm (UBCHyst) to 24 cm (PM4Sand) and for a T_R of 2475 years, the displacements from analytical procedures ranges from 0 cm to 8.2 cm (PSDA) whereas the displacement from NDA varies from 12 cm (Wang 2D) to 44 cm (PM4Sand). The lower

displacements obtained from analytical procedures corresponds to the following: 1) The analytical procedures used in this study are formulated to only capture the deviatoric mechanisms associated with shear-induced deformations, and they do not capture volumetric mechanism. On the other hand, the displacements estimated using numerical models capture both the volumetric and deviatoric mechanisms. 2) The displacements calculated using advanced numerical analyses incorporate better the physics involved in the estimation of seismically-induced displacements; whereas, the analytical models include several simplifications to allow efficient computation using a large number of ground motions. For example, the stick slip model is based on a generalized single degree of freedom model and the transfer function model, is based on transfer functions.

Table 4 Comparison of displacements for a selected return period.

Return period	Analytical methods			Numerical Analysis		
	PSDA	Stick-slip	Transfer Function	UBCHyst	PM4Sand	Wang 2D
475 years	1.5 cm	0	0	5 cm	24 cm	7 cm
2475 years	8.2 cm	1.6 cm	0	18 cm	44 cm	12 cm

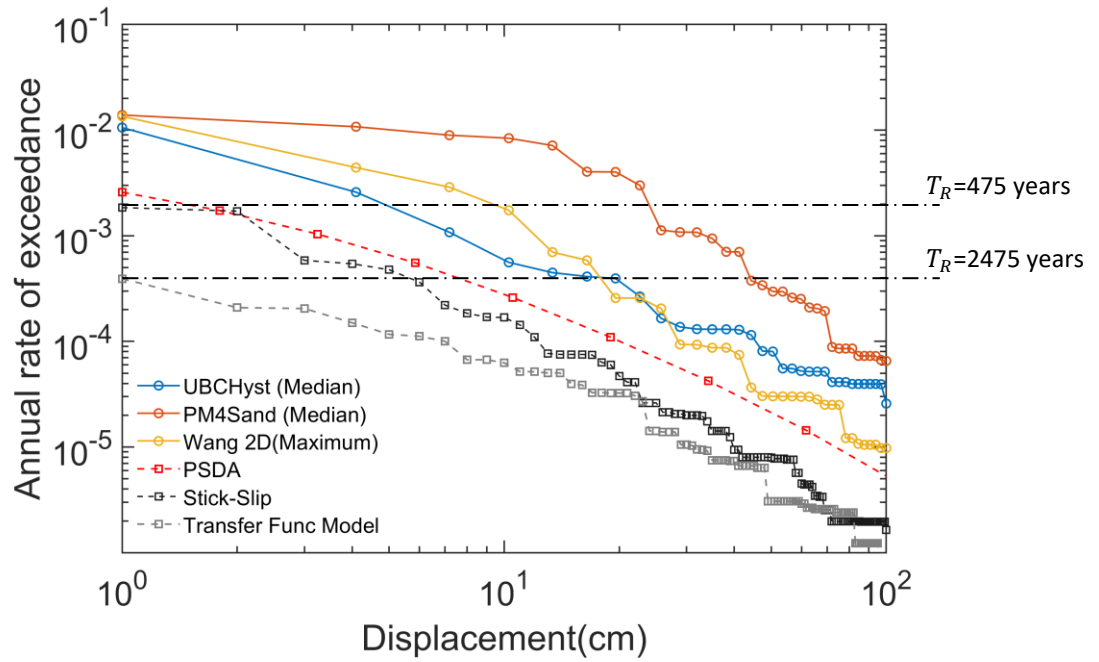


Figure 6-12 Comparison of displacement hazard curves from analytical methods and nonlinear dynamic analyses.

CHAPTER 7. SUMMARY OF FINDINGS AND CONCLUSIONS

The current state of practice in the seismic performance assessment of rockfill dams is dominated by pseudoprobabilistic procedures, at least in initial design stages, in which the estimation of engineering demand parameters of interest for a dam system (e.g., the amount of seismically-induced displacements) is separated from the estimation of the ground motion hazard. In contrast, in a performance-based framework, the engineers can directly get the displacement associated with a selected design hazard level. Performance-based procedures are more robust because they consider the full hazard curve of an intensity measure of interest. Further, a performance-based procedure provides seismically-induced displacement estimates that are consistent with a design hazard level (or return period). Hence, they should be used in practice.

Previous efforts have implemented analytical procedures to estimate seismically-induced displacements in a performance-based framework. These procedures rely on simplifications that can allow running a large number of ground-motions in a computationally efficient manner. These analytical procedures have been formulated to account only for the deviatoric component of the seismically-induced displacements. There have not been previous attempts that the author is aware of for evaluating how these procedures compare against advanced numerical analyses, which can better capture the physics involved in the generation of seismically-induced displacements. One challenge in using advanced numerical analyses is that they are much more computationally expensive. In this study, we proposed using the conditional scenario spectra (CSS) approach combined with advanced numerical analyses to estimate displacement hazard curves that can be used

as benchmarks for the evaluation of simplified and analytical procedures that provide estimates of seismically-induced displacements in rockfill dams.

It is shown that using the CSS approach, the ground motion hazard at a given site can be recovered directly from a selected set of ground motions, using rate of occurrences assigned to each ground-motions. The main challenge in using the CSS approach is the need to perform advanced numerical analyses with a large suite of ground-motions, which is computationally expensive. In this study, this was feasible by parallel computation. These types of calculations are still challenging in engineering practice due to the large computational resources that are required.

The comparisons between performance-based assessments that rely on simplified, analytical, and advanced numerical modeling were performed by conducting advanced numerical nonlinear analyses that used the CSS-based selected ground motions on a rockfill dam. The comparisons were performed in terms of displacement hazard curves. It is shown that the analytical methods underpredict the displacement for a selected hazard level. This is because the analytical methods are formulated only to capture deviatoric mechanisms, whereas the advanced numerical analyses integrate better the strain-dependent modulus reduction, damping, and volumetric behavior of the material.

Three different constitutive models were used in performing the advanced numerical analyses (UBCHyst, PM4Sand, Wang 2D). The constitutive models have been calibrated against modulus reduction and damping curves of rockfill materials obtained from the literature. For the constitutive models formulated for sands but applied to rockfills in this study, a zero generation of excess pore pressures were imposed. In addition, the model

parameters were focused on capturing representative modulus reduction and damping curves of rockfill materials. The comparisons of displacements obtained from the three constitutive models have been performed in terms of displacement hazard curves. The PM4Sand model produces the highest displacement for a selected hazard level as it has the highest contribution from volumetric mechanisms because of the contractive behavior. Wang 2D models shows the lowest displacements for a selected hazard level as it exhibits higher damping ratios comparatively. In addition to the strain-dependent behavior, the complex nonlinear dynamic analyses also combine the stress-dependent behavior of the models. For example, the behavior of the constitutive models at the crest area, where the vertical confinement is lower, is different from the behavior of the models inside the fill. In the crest area, the vertical displacement hazard curve from PM4Sand model is below UBCHyst model for high displacement thresholds because of the dilative behavior exhibited by the model at a lower confinement.

When considering the UBCHyst model, the displacement estimates from numerical analyses were about 2 to 3 times the estimates from the PSDA and stick-slip models, and this ratio was stable across different hazard levels. The displacement estimates were about 5 times higher than those from the TFM model. These ratios increased for the PM4Sand model and decreased for the Wang model. This is because the PM4Sand model provides a larger contribution to volumetric mechanisms, whereas the Wang model has a lower contribution to volumetric mechanisms and also shows larger damping.

In terms of future work, we suggest considering the following. Most of the modern simplified methods (either based on predictive equations or analytical models) capture only shearing mechanisms. The author is not aware of any modern methods to capture the

contribution from volumetric mechanisms. The method proposed by Tokimatsu and Seed (1987) is still used nowadays to estimate volumetric-induced settlements and should be updated to include the recent advances in geotechnical earthquake engineering. Future work should also consider developing a robust constitutive model to capture the response of rockfill materials. In this study, the calibrations were focused on representing the modulus reduction and damping behavior, which is an accepted practice in the assessment of rockfill materials but other aspects in the seismic response of rockfill materials should be included (e.g., dilatancy). Finally, this study was focused on reproducing the hazard associated with S_a , future studies should consider reproducing not only the S_a hazard but also the hazard associated with other intensity measures.

REFERENCES

- Abrahamson, N. A. (2017). "HAZ45 computer program." Version 45.3
- Abrahamson, N. A., Silva, W. J., Kamai, R. (2014). "Summary of Abrahamson & Silva NGA Ground-Motion Relation for Active Crustal Regions." *Earthquake Spectra*, 30(3), 1025-1055
- Acar, M., Numanoglu, O. A., Hashash, Y. M. A. (2019). Numerical Simulation of Dynamic Centrifuge Tests on Concrete Faced Rockfill Dam. *Geo-Congress 2019*. doi:10.1061/9780784482100.012
- Ancheta, T. D., Darragh, R. B., Stewart, J. P., Seyhan, E., Silva, W. J., Chiou, B. S. -J., Wooddell, K. E., Graves, R. W., Kottke, A. R., Boore, D. M., Kishida, T., and Donahue, J. L., (2014). NGA-West2 database, *Earthquake Spectra* 30, 989–1005.
- Armstrong, R., Kishida, T., Park, D. (2020). Efficiency of ground motion intensity measures with earthquake-induced earth dam deformations. *Earthquake Spectra*, 875529302093881. doi:10.1177/8755293020938811
- Arteta, C. A., Abrahamson, N. A. (2019). Conditional Scenario Spectra (CSS) for Hazard-Consistent Analysis of Engineering Systems. *Earthquake Spectra*, 35(2), 737–757. doi:10.1193/102116eqs176m
- Baker, J. W. (2011). Conditional Mean Spectrum: Tool for Ground-Motion Selection. *Journal of Structural Engineering*, 137(3), 322–331. doi:10.1061/(asce)st.1943-541x.0000215
- Baker, J. W., Jayaram, N. (2008). Correlation of Spectral Acceleration Values from NGA Ground Motion Models. *Earthquake Spectra*, 24(1), 299–317. doi:10.1193/1.2857544
- Bayraktar, A., Kartal, M. E. (2010). Linear and nonlinear response of concrete slab on CFR dam during earthquake. *Soil Dynamics and Earthquake Engineering*, 30(10), 990-1003.
- Bolton, M. D. (1986). "The strength and dilatancy of sands." *Geotechnique* 36, No. 1, 65-78.
- Boore D.M., Stewart J.P., Seyhan E., Atkinson G.M. (2014). "NGA-West 2 Equations for Predicting PGA, PGV, and 5%-Damped PSA for Shallow Crustal Earthquakes." *Earthquake Spectra*, 30(3): 1057–1085.

Boulanger, R. W., Ziotopoulou, K. (2017). "PM4Sand (version 3.1): A sand plasticity model for earthquake engineering applications." Report No. UCD/CGM-17/01, Center for Geotechnical Modeling, Department of Civil and Environmental Engineering, University of California, Davis, CA, March, 114 pp.

Bray, J. D., Macedo, J. (2019a). Procedure for Estimating Shear-Induced Seismic Slope Displacement for Shallow Crustal Earthquakes. *Journal of Geotechnical and Geoenvironmental Engineering*, 145(12), 04019106. doi:10.1061/(asce)gt.1943-5606.0002143

Bray, J. D., Travararou, T. (2007). Simplified Procedure for Estimating Earthquake-Induced Deviatoric Slope Displacements. *Journal of Geotechnical and Geoenvironmental Engineering*, 133(4), 381–392. doi:10.1061/(asce)1090-0241(2007)133:4(381)

Bray, J. D., Macedo, J., Travararou, T. (2018). Simplified Procedure for Estimating Seismic Slope Displacements for Subduction Zone Earthquakes. *Journal of Geotechnical and Geoenvironmental Engineering*, 144(3), 04017124. doi:10.1061/(asce)gt.1943-5606.0001833

Bray, J., Macedo, J. (2018a) Evaluating liquefaction-induced building settlements. 11th National conference on earthquake engineering; Los Angeles, California.

Bray, J., Macedo, J. (2018b). Assessment of liquefaction induced building settlement. 2018 NZSEE conference, New Zealand Society for Earthquake Engineering.

Bray, J., Macedo, J. (2018c). Simplified evaluation of liquefaction-induced building settlements. *Geotechnical earthquake engineering and soil dynamics V*; Austin, Texas.

Bray, J., Macedo, J. (2019b). Shear-induced seismic slope displacement estimates for shallow crustal earthquakes. 7th International Conference on Earthquake Geotechnical Engineering; Rome, Italy.

Bray, J., Macedo, J., Luque, R. (2017). Key trends in assessment of liquefaction-induced building settlement. 3rd International conference on performance-based design in earthquake geotechnical engineering; Vancouver, Canada.

Bray, J.D., Macedo, J., (2017a). 6th Ishihara lecture: Simplified procedure for estimating liquefaction-induced building settlement. *Soil Dynamics and Earthquake Engineering*, 102, pp.215–231.

- Bray, J., Macedo, J. (2017b). Simplified procedure for estimating liquefaction-induced building settlements. Ishihara lecture. 19th International Conference on Soil Mechanics and Geotechnical Engineering; Seoul, Korea.
- Campbell K.W., Bozorgnia Y. (2014). “NGA-West2 Ground Motion Model for the Average Horizontal Components of PGA, PGV, and 5% Damped Linear Acceleration Response Spectra.” *Earthquake Spectra*, 30(3): 1087–1115.
- Candia, G., Macedo, J., Jaimes, M. A., Magna-Verdugo, C. (2019a). A New State-of-the-Art Platform for Probabilistic and Deterministic Seismic Hazard Assessment. *Seismological Research Letters*, 90(6), 2262–2275. doi:10.1785/0220190025
- Candia, G., Macedo, J., Jaimes, M., Magna, C. (2019b). A computational platform for the quantification of the seismic demand in mining projects. Tailings and mine waste 2019 conference; Vancouver, Canada.
- Candia, G., Macedo, J., Magna, C. (2018). An integrated platform for seismic hazard assessment in subduction zones. 11th National conference on earthquake engineering; Los Angeles, California.
- Chowdhury, K.H. (2018). Evaluation of the State of Practice regarding Nonlinear Seismic Deformation Analyses of Embankment Dams Subject to Soil Liquefaction Based on Case Histories. PhD Dissertation, University of California, Berkeley.
- Dafalias, Y. F., Manzari, M. T. (2004). Simple Plasticity Sand Model Accounting for Fabric Change Effects. *Journal of Engineering Mechanics*, 130(6), 622–634. doi:10.1061/(asce)0733-9399(2004)130:6(622)
- Hale, C. (2019). A Transfer Function Model for Deformation Hazard Analysis of Earthen Dams." PhD Dissertation, University of California, Berkeley.
- Han, B., Zdravkovic, L., Kontoe, S., Taborda, D. M. G. (2016). Numerical investigation of the response of the Yele rockfill dam during the 2008 Wenchuan earthquake. *Soil Dynamics and Earthquake Engineering*, 88, 124–142. doi:10.1016/j.soildyn.2016.06.002
- Hudson, M. B., Idriss, I. M., Beikae, M. (2003). QUAD4MU: Addendum to user’s manual for QUAD4M for updates to the QUAD4MU version. March 4, 2003.
- Idriss, I. M. (2014). “An NGA-West2 Empirical Model for Estimating the Horizontal Spectral Values Generated by Shallow Crustal Earthquakes.” *Earthquake Spectra*, 30(3), 1155-1177

Itasca Consulting Group (2016) FLAC, Fast Lagrangian Analysis of Continua, User's Guide, Version 8.0. Minneapolis, MN: Itasca Consulting Group.

Kishida, T., Park, D., Sousa, R. L., Armstrong, R., Byon, Y.-J. (2019). Modulus reductions of dam embankment materials based on downhole array time series. *Earthquake Spectra*, 36(1), 400–421. doi:10.1177/8755293019878182

Kuhlemeyer, R.L., Lysmer, J. (1973) Finite element method accuracy for wave propagation problems. *Journal of the Soil Mechanics and Foundations Division* 99(SM5): 421–427.

Li, H., Chi, S., Lin, G., Zhong, H. (2008). A modified approach for determination of nonlinear properties in seismic response analyses for 200 m high core rock-fill dams. *Canadian Geotechnical Journal*, 45(8), 1064–1072. doi:10.1139/t08-045

Macedo, J. (2017). Simplified procedures for estimating earthquake-induced displacements. PhD Dissertation, University of California, Berkeley.

Macedo, J., Bray, J. D. (2018a). Key Trends in Liquefaction-Induced Building Settlement. *Journal of Geotechnical and Geoenvironmental Engineering*, 144(11), 04018076. doi:10.1061/(asce)gt.1943-5606.0001951

Macedo, J., Bray, J., Abrahamson, N., Travararou, T. (2018). Performance-based probabilistic seismic slope displacement procedure. *Earthquake Spectra (EERI)*; 34(2):673-695. <https://doi.org/10.1193/122516EQS251M>.

Macedo, J., Bray, J., Abrahamson, N., Travararou, T. (2017a). Probabilistic simplified seismic performance assessment of earth slopes and geotechnical structures. 3rd International Conference on Performance-based Design in Earthquake Geotechnical Engineering; Vancouver, Canada.

Macedo, J., Candia, G. (2020). Performance-based assessment of the seismic pseudo-static coefficient used in slope stability analysis. *Soil Dynamics and Earthquake Engineering*, 133, 106109. doi:10.1016/j.soildyn.2020.106109

Macedo, J., Abrahamson, N., Liu, C. (2020a). New Scenario-Based Cumulative Absolute Velocity Models for Shallow Crustal Tectonic Settings. *Bulletin of the Seismological Society of America*. doi:10.1785/0120190321

Macedo, J., Aguilar, Z. (2012) Seismic calibration of an instrumented earth dam in terms of response spectra. In: *Proceedings of the 15th World Conference on Earthquake Engineering*, October. Lisbon, Portugal.

Macedo, J., Bray, J. (2018b). Insights from numerical analysis of liquefaction-induced building settlement. In: Is-Atlanta and B2G-Atlanta conference; Atlanta, Georgia.

Macedo, J., Bray, J., Travasarou, T. (2017b) Simplified procedure for estimating seismic slope displacements in subduction zones. In: Proceedings of the 16th World Conference on Earthquake Engineering, 2017.

Macedo, J., Candia, G. (2019a). Performance-based assessment of seismically-induced slope displacements in tailings dams. Tailings and mine waste 2019 conference; Vancouver, Canada.

Macedo, J., Candia, G. (2019b). Performance-based assessment of the seismic pseudostatic coefficient in mining projects. Tailings and mine waste 2019 conference; Vancouver, Canada.

Macedo, J., Candia, G., Abrahamson, N. (2020b). A computational platform for the assessment of seismically-induced slope displacements. Geo-Congress 2020, Minneapolis.

Macedo, J., Candia, G., Lacour, M., Liu, C. (2020c). New developments for the performance-based assessment of seismically-induced slope displacements. *Engineering Geology*, 277, 105786. doi:10.1016/j.enggeo.2020.105786

Macedo, J., Lacour, M., Abrahamson, N. (2020d). Epistemic uncertainty treatment in seismically-induced slope displacements using polynomial chaos. *Journal of Geotechnical and Geoenvironmental Engineering (ASCE/JGGE)*; 146(10). [https://doi.org/10.1061/\(ASCE\)GT.1943-5606.0002345](https://doi.org/10.1061/(ASCE)GT.1943-5606.0002345).

Macedo, J., Zuta, J., Aguilar, Z. (2015) Numerical seismic analysis of an instrumented earth dam in terms of the variability of the response design spectra. In: Proceedings of the 6th International Conference on Earthquake Geotechnical Engineering.

Macedo, J., Aguilar, Z. (2011). Calibration of a dynamic model for Yuracmayo earth dam. 5th International Conference on Geotechnical Earthquake Engineering; Santiago, Chile.

Macedo, J., Aguilar, Z., Zuta, J. (2010). Dynamic analysis of Yuracmayo earth dam. 14th European Conference on Earthquake Engineering; Ohrid, Republic of Macedonia.

Makdisi, F. I., Seed, H. B. (1978). Simplified procedure for estimating dam and embankment earthquake-induced deformations. *J. Geotech. Geoenviron. Eng.*, 104(7): 849-867.

- Marulanda, C., Marulanda, A. (2015). CFRD: past and present (*). In 25th international congress on large dams. Stavanger, Norway: International Commission on Large Dams.
- Matsumoto, N. (2010). The Recent Earthquakes and Dam Safety in Japan. International Commission on Large Dams Symposium.
- Naesgaard, E., Byrne, P. (2011). Hysteretic Model for Non-liquefiable Soils (UBCHYST5d). UBCHYST5d Memo.
- Naesgaard, E., Byrne, P., Amini, A (2015). Hysteretic Model for Non-liquefiable Soils (UBCHYST5d). <https://www.itscainternational.com/software/udm-library/masquerade>
- Newmark, N. M. (1965). Effects of Earthquakes on Dams and Embankments, *Géotechnique*, 15(2): 139-160.
- Park, D., Kishida, T. (2019). Seismic Response of Embankment Dams Based on Recorded Strong-Motion Data in Japan. *Earthquake Spectra*, 35(2), 955–976. doi:10.1193/042918eqs107m
- Park, D., Kishida, T. (2019). Seismic Response of Embankment Dams Based on Recorded Strong-Motion Data in Japan. *Earthquake Spectra*, 35(2), 955–976. doi:10.1193/042918eqs107m
- Rathje, E. M., Bray, J. D. (2000). Nonlinear Coupled Seismic Sliding Analysis of Earth Structures. *Journal of Geotechnical and Geoenvironmental Engineering*, 126(11), 1002–1014. doi:10.1061/(asce)1090-0241(2000)126:11(1002)
- Rathje, E. M., Saygili, G. (2009). Probabilistic assessment of earthquake-induced sliding displacements of natural slopes. *Bulletin of the New Zealand Society for Earthquake Engineering*, 42(1), 18–27. doi:10.5459/bnzsee.42.1.18-27
- Rathje, E. M., Wang, Y., Stafford, P. J., Antonakos, G., Saygili, G. (2013). Probabilistic assessment of the seismic performance of earth slopes. *Bulletin of Earthquake Engineering*, 12(3), 1071–1090. doi:10.1007/s10518-013-9485-9
- Rocscience (2018). Critical seismic coefficient analysis in Slide. Rocscience, Toronto, Ontario, CA.
- Rollins, K. M., Evans, M. D., Diehl, N. B., Daily, W. D. I. (1998). Shear modulus and damping relationships for gravels. *J. Geotech. Geoenviron Engng*124, No. 5, 396–405

Rollins, K. M., Singh, M., Roy, J. (2020). Simplified Equations for Shear-Modulus Degradation and Damping of Gravels. *Journal of Geotechnical and Geoenvironmental Engineering*, 146(9), 04020076. doi:10.1061/(asce)gt.1943-5606.0002300

Saygili, G., Rathje, E. M. (2008). Empirical Predictive Models for Earthquake-Induced Sliding Displacements of Slopes. *Journal of Geotechnical and Geoenvironmental Engineering*, 134(6), 790–803. doi:10.1061/(asce)1090-0241(2008)134:6(790)

Seed, H. B., Wong, R., Idriss, I., Tokimatsu, K. (1986). Moduli and damping factors for dynamic analyses of cohesionless soils. *J. Geotech. Engng* 112, No. 11, 1016–1032.

Seed, H.B., K.L. Lee, I.M. Idriss., F. Makdisi. (1973). Analysis of the Slides in the San Fernando Dams During the Earthquake of Feb. 9, 1971. EERC 73-2. Berkeley, California: Earthquake Engineering Research Center.

Seo, M. W., Ha, I. S., Kim, Y. S., Olson, S. M. (2009). Behavior of concrete-faced rockfill dams during initial impoundment. *Journal of geotechnical and geoenvironmental engineering*, 135(8), 1070-1081.

Stewart JP, Bray JD, McMahon DJ, Smith PM, Kropp AL (2001) Seismic performance of hillside falls. *Journal of Geotechnical and Geoenvironmental Engineering ASCE* 127(11):905–919.

Tokimatsu, K., Seed, H. B. (1987). Evaluation of Settlements in Sands Due to Earthquake Shaking. *Journal of Geotechnical Engineering*, 113(8), 861–878. doi:10.1061/(asce)0733-9410(1987)113:8(861)

Wang, Z., Dafalias, Y. F., Shen, C. (1990). Bounding Surface Hypoplasticity Model for Sand. *Journal of Engineering Mechanics*, 116(5), 983–1001. doi:10.1061/(asce)0733-9399(1990)116:5(983)

Wang, Z.L. (1990). Bounding Surface Hypo-Plasticity Model for Granular Soils and Its Application. Ph.D. dissertation, University of California at Davis.

Wang, Z.-L., Ma, F. (2018). “Wang2D: A plasticity sand model updated based on simple shear test data.” <https://www.itascacg.com/udms/wang2d>

Wartman, J., Bray, J. D., Seed, R. B. (2003). Inclined Plane Studies of the Newmark Sliding Block Procedure. *Journal of Geotechnical and Geoenvironmental Engineering*, 129(8), 673–684. doi:10.1061/(asce)1090-0241(2003)129:8(673)

Wen, L., Chai, J., Xu, Z., Qin, Y., Li, Y. (2017). Monitoring and numerical analysis of behavior of Miaojiaba concrete-face rockfill dam built on river gravel foundation in China. *Computers and Geotechnics*, 85, 230–248. <https://doi.org/10.1016/j.compgeo.2016.12.018>

Wilson, R.C., Keefer, D.K., 1985, Predicting areal limits of earthquake-induced landsliding, in J.I. Ziony, editor, *Evaluating earthquake hazards in the Los Angeles region-an earth-science perspective: U.S. Geological Survey Professional Paper 1360*, p. 317-345.

Youd, T. L. (1978). "Major Cause of Earthquake Damage Is Ground Failure." *Civil Engineering Magazine*, ASCE, vol. 48, no. 4, pp. 47–51.

Zhou, W., Chen, Y., Ma, G., Yang, L., Chang, X. (2017). A modified dynamic shear modulus model for rockfill materials under a wide range of shear strain amplitudes. *Soil Dynamics and Earthquake Engineering*, 92, 229–238. doi:10.1016/j.soildyn.2016.10.027

Zhu, S., Yang, G., Wen, Y., Ou, L. (2014). Dynamic shear modulus reduction and damping under high confining pressures for gravels. *Géotechnique Letters*, 4(3), 179–186. doi:10.1680/geolett.14.00030